



LAWRENCE  
LIVERMORE  
NATIONAL  
LABORATORY

# On the Origin of Ultra High Energy Cosmic Rays

T.K. Fowler, S. Colgate, H. Li

July 2, 2009

## **Disclaimer**

---

This document was prepared as an account of work sponsored by an agency of the United States government. Neither the United States government nor Lawrence Livermore National Security, LLC, nor any of their employees makes any warranty, expressed or implied, or assumes any legal liability or responsibility for the accuracy, completeness, or usefulness of any information, apparatus, product, or process disclosed, or represents that its use would not infringe privately owned rights. Reference herein to any specific commercial product, process, or service by trade name, trademark, manufacturer, or otherwise does not necessarily constitute or imply its endorsement, recommendation, or favoring by the United States government or Lawrence Livermore National Security, LLC. The views and opinions of authors expressed herein do not necessarily state or reflect those of the United States government or Lawrence Livermore National Security, LLC, and shall not be used for advertising or product endorsement purposes.

This work performed under the auspices of the U.S. Department of Energy by Lawrence Livermore National Laboratory under Contract DE-AC52-07NA27344.

# On the Origin of Ultra High Energy Cosmic Rays

T. Kenneth Fowler, Lawrence Livermore National Laboratory\*

Stirling Colgate and Hui Li, Los Alamos National Laboratory

## Abstract

Turbulence-driven plasma accelerators produced by magnetized accretion disks around black holes are proposed as the mechanism mainly responsible for observed cosmic ray protons with ultra high energies  $10^{19} - 10^{21}$  eV. The magnetized disk produces a voltage comparable to these cosmic ray energies. Here we present a Poynting model in which this voltage provides all of the energy to create the jet-like structures observed to be ejected from accretion disks, and this voltage also accelerates ions to high energies at the top of the expanding structure. Since the inductive electric field  $\mathbf{E} = -\mathbf{v} \times \mathbf{B}$  driving expansion has no component parallel to the magnetic field  $\mathbf{B}$ , ion acceleration requires plasma wave generation – either a coherent wave accelerator as recently proposed, or instability-driven turbulence. We find that turbulence can tap the full inductive voltage as a quasi-steady accelerator, and even higher energies are produced by transient events on this structure. We find that both MHD modes due to the current and ion diffusion due to kinetic instability caused by the non-Maxwellian ion distribution contribute to acceleration. We apply our results to extragalactic giant radiolobes, whose synchrotron emissions serve to calibrate the model, and we discuss extrapolating to other astrophysical structures. Approximate calculations of the cosmic ray intensity and energy spectrum are in rough agreement with data and serve to motivate more extensive MHD and kinetic simulations of turbulence that could provide more accurate cosmic ray and synchrotron spectra to be compared with observations. A distinctive difference from previous models is that the cosmic ray and synchrotron emissions arise from different parts of the magnetic structure, thus providing a signature for the model.

\*Consultant, University of California, Berkeley, e-mail: fowler@nuc.berkeley.edu

## TABLE OF CONTENTS

Section 1	Introduction
Section 2	Qualitative Features
Section 3	Current Generation
Section 4	Evolution of the Magnetic Structure: MHD Simulations
Section 5	Evolution of the Magnetic Structure: Theoretical Model
Section 6	Electron Synchrotron Radiation
Section 7	Quasi-Steady Ion Acceleration
Section 8	Quasi-Steady Cosmic Ray Spectrum
Section 9	Ion Acceleration by Transient Events: Ultra Ultra High Energies
Section 10	Reverse Polarity, Electron Acceleration, Scaling
Section 11	Conclusions, Future Work
Appendix A	Plasma Physics Topics
Appendix A1	Current Generation, Plasma Density
Appendix A2	Helicity Injection
Appendix A3	Magnetic Relaxation and Hyper-Resistivity
Appendix A4	Current Filamentation in the Central Column
Appendix A5	Electron Scattering
Appendix A6	Transport and Acceleration by Tangled Magnetic Fields
Appendix A7	Transport by Drift Cyclotron Modes
References	
Figure 1	

## 1. Introduction

The conjecture that ultra high energy cosmic ray protons with energies  $10^{19} - 10^{20}$  eV arise from Active Galactic Nuclei has recently been substantiated [1]. Jets ejected from AGN's have been proposed as the source of acceleration energy, both kinetic and magnetic forces having been postulated to drive the jet-like ejections from AGN's [2].

Here we follow the magnetic hypothesis, or Poynting model, in which a magnetic field alone creates jets that accelerate cosmic ray ions, yielding features markedly different from kinetic models. We extend the work of Colgate and Li in which giant radiolobes produced by AGN's are assumed to be magnetic structures like “spheromak” plasmas produced in the laboratory [3]. We arrive at a self-consistent model, yielding both the observed synchrotron radiation and also the acceleration and ejection of ultra-energetic ions as cosmic rays. Our model, based on plasma turbulence as distinct from coherent plasma wave acceleration recently proposed [4], yields numbers in rough agreement with several aspects of the astrophysical data on giant radiolobes.

An example jet/radiolobe magnetic structure obtained by MHD simulation is shown in Fig. 1 taken from Ref. [5], showing a rising column of current that flares out at the top where field lines turn radially to make their way back to the source. Figures in that reference closely resemble “spheromaks” produced by plasma guns, much studied in magnetic fusion energy research. As in spheromaks, plasma instability actually creates the 3D structure also shown in Ref. [5], the 2D figures being the toroidal average of the 3D figures.

In Section 2, we apply results from spheromak research and other plasmas physics results to predict the main features of giant radiolobe structures and cosmic ray acceleration produced by these structures. Sections 2 – 9 describe a detailed model having these features, as one example demonstrating self-consistency of the concepts, including in Section 6 the observed electron synchrotron radiation from giant radiolobes that serves to calibrate model parameters. Extrapolation of the giant radiolobe model to other astrophysical objects is discussed in Section 10, and future work needed to pin down details of both cosmic ray and synchrotron spectra is described in Section 11. To maintain narrative flow, discussions of relevant plasma physics topics are collected in Appendix A. We use MKS units, giving cosmic ray energies in electron volts.

## 2. Qualitative Features

Results in Ref. [5] simulating giant radiolobe formation could equally well describe the formation of spheromaks in the laboratory, merely by replacing the magnetic flux generator of Ref. [5] by an electrostatic plasma gun with applied voltage  $V$ , as in the pioneering work of Ref. [6] and many subsequent papers in the plasma physics literature. For a spinning disk of active radius  $a_o$ , and magnetic field  $B_o$  perpendicular to the disk,  $V = a_o (v_o \times B_o)$  with an electromotive force  $v_o \times B_o$  for rim speed  $v_o$ . In Section 4 and Appendix A1, we show that this voltage can produce an electric acceleration greatly exceeding the gravitational attraction of the black hole. Then electric currents can arise outside the event horizon, described, in an inertial reference frame centered in the disk, by:

$$-\partial \mathbf{B} / \partial t = \nabla \times \mathbf{E} \quad (1)$$

$$\mathbf{j} \times \mathbf{B} = \nabla \cdot \mathbf{P} \quad (2)$$

where  $\mathbf{j}$  is the current density.

We will find that the rate of magnetic expansion is slow compared to the Alfven speed, whereby the momentum equation can be replaced by the equilibrium Eq. (2) with pressure tensor  $\mathbf{P}$  discussed below. The slow dynamic driver is the electric field  $\mathbf{E}$ , given inside the current channel by:

$$\mathbf{E} = -\mathbf{v} \times \mathbf{B} \quad (3)$$

where  $\mathbf{v}$  is the fluid velocity and for the moment we neglect dissipation. Thus the dynamics is described by a succession of equilibria expanding slowly at a rate  $v \approx dL/dt$  where  $L$  is the vertical length of the structure.

It is well known from the study of spheromaks that these equilibria always look like those of Ref. [5], with a central column of current terminated by a return current and

magnetic flux that takes the shape of a confining boundary in most laboratory experiments [6]. For accretion disks, external pressure around the disk determines the shape of the jet, which expands to a large size as pressure drops away from the disk [2, 5]. However, external pressure is too weak to oppose the strong magnetic pressure at the upper boundary or “nose” of the structure, so that the length  $L$  expands freely as long as the disk can feed energy to expansion. The main effect slowing down expansion is the growing magnetic energy inside the lobe, easily calculable since the field there is essentially the vacuum field due to current in the central column (as seen in Fig. 1C showing  $B \propto 1/r$  inside the lobe). Compared to earlier work [7],  $dL/dt$  is reduced by a factor  $\ln(R/a_0) \approx 20$  for a lobe of radius  $R$  (see Section 5).

The radius of the central column depends on the pressure tensor  $\mathbf{P}$ . This is the main distinguishing feature of our model, compared with kinetic models such as the magnetocentrifugal model of Ref. [8] in which  $\mathbf{P}$  includes an ad hoc injection of mass near the axis of symmetry. By contrast, we replace mass injection by a boundary condition that injects electric current, as in Ref. [6] describing electrostatic plasma gun injection. We have in mind a physical situation in which ions carrying current are extracted through an electrostatic sheath, as in a plasma gun, while the growing jet/radiolobe structure shields itself from additional mass accretion inside the lobe. Further expansion of the radiolobe is driven solely by the voltage drop across the lobe where it intersects the spinning magnetized disk. This voltage is so large that all ions carry current at speed  $c$ , giving a density  $n \propto (I/ec)$ , as discussed in Sections 3 and 6, and in some detail in Appendix A1.

Since the mass injected into the radiolobe in our model is just that required to carry the current, we will find that  $\mathbf{P}$  in the central column is small because the density  $n$  is small. Setting  $\mathbf{P} = 0$  in Eq. (2) gives a “force free” equilibrium, for which the central column radius is about equal to the active disk radius  $a_0$ . But the disk radius will turn out to be orders of magnitude smaller than that of the visible jet.

Thus, in contrast with kinetic models favoring a continuous structure filling the visible domain of the observed jet/radiolobe, our purely Poynting model predicts that the central column of current is a very thin filament deep inside the visible boundary that surrounds a largely empty radiolobe. Also, because the column radius is small, the

magnetic field is very high inside the filament, giving enhanced synchrotron radiation. Then the apparent continuous glow of the radiolobe is actually due to synchrotron radiation from the thin filament inside. Because of instability, the thin filament is twisted so as to loosely fill the volume, shown in Ref. [5]. The extended glow arises from the twisted filament, as in an incandescent light bulb. With adequate resolution to see it, this filamentary structure would provide a distinguishing feature of the model.

For cosmic rays, an important consequence of the filamentary central column is the fact that strong synchrotron radiation by the ions could prevent the acceleration of ions to high energies, even though the unstable twisting of the column does provide an accelerating voltage along field lines of the toroidally-averaged field structure. We find that, while large transient events can overcome radiation, acceleration by quasi-steady levels of turbulence that explains much of the data is only overcome as field lines bend and diverge to form the return flux at the nose.

Thus we are led to a model in which quasi-steady ion acceleration occurs only in the extreme nose, where flux expansion reduces the magnetic field to the point that synchrotron radiation is no longer dominant. The filamentary central column serves mainly to transmit energy to the distant nose largely undiminished. If acceleration does occur in the nose, the increasing ion pressure due to acceleration finally exceeds the weak magnetic pressure, causing the flux return to widen. This is a kinetic effect, not captured in MHD simulations. Moreover, acceleration to the highest energies is almost surely due to a kinetically-driven instability. The reason for this is that, as the flux return widens, the dominant magnetic field is toroidal (around the axis of symmetry), while the current is mainly poloidal, flowing in the plane of figures of Ref. [5], perpendicular to the toroidal field lines. Then particles carrying the current must flow perpendicular to the field, and this requires instability to produce diffusion across the magnetic field giving strong acceleration of the ions. Instability-driven acceleration was also proposed in Ref. [9].

Fortunately for the model, we will find a confluence of circumstances whereby kinetic instability of the ions sets in just when it is required to carry the current. Details are developed in Section 7, and acceleration by transient events in the central column is discussed in Section 9. The predicted spectrum of cosmic ray energies by all processes is discussed in Section 8, and found to be in reasonable agreement with observations.



Details of the magnetic structure model are developed in Sections 5 and 6 and the self-consistency of model parameters with observed electron synchrotron radiation is discussed in Section 6. Three other points of self-consistency are: (1) the current profile used to calculate magnetic energy, (2) unstable diffusion of electrons enhancing synchrotron radiation in the central column, and (3) the existence of mechanisms for ion diffusion where it is needed in the “nose.” The latter two points are discussed in Sections 6 and Appendix A5 for point (2) and Section 7 and Appendix A7 for point (3).

Concerning point (1), fortunately details of the current profile are not very important in calculating the magnetic energy. For concreteness we will assume magnetic relaxation that would distribute current across the central column and across the flux return [10]. We will find this to be well justified in the flux return and marginally so in the central column. However, the opposite extreme in which current flows as a “skin” current in the absence of relaxation still gives about the same magnetic energy inside the column, as discussed in Appendix A3.

In the laboratory, the timescale for magnetic relaxation is usually given by collisional resistance, while resistance is negligible here. Instead, relaxation of the 2D-averaged magnetic field structure is due to 3D instability giving the results in Ref. [5] for the case of MHD instability. Taking the fields in Eq. (1) to be 2D averages, relaxation of the 2D averaged  $\mathbf{B}$  is caused by a 2D averaged  $\mathbf{E}$  due to instability and a corresponding voltage drop  $\Delta V$ . Substituting the 2D averaged  $\mathbf{E}$  into Eq. (1) gives a magnetic relaxation time comparable to  $\tau$ , the radiolobe lifetime. The existence of the 2D averaged  $\mathbf{E}$  due to current-driven instability was demonstrated for MHD simulations in Ref. [6].

### 3. Current Generation

In order for Poynting flux to generate a giant radiolobe magnetic structure, accretion must produce a coherent magnetic field embedded in the spinning disk [3]. It is the coherent field discussed in Ref. [3] that serves to determine the orientation of the axis of symmetry of the figures in Ref. [5]. Here we assume that an embedded field exists and examine the consequences.

We continue to adopt an inertial reference frame centered in the spinning accretion disk. In this reference frame, an embedded magnetic field  $\mathbf{B}$  normal to the disk

produces a voltage  $V$  found by integrating the electric field  $\mathbf{v} \times \mathbf{B}$  across the disk, where  $\mathbf{v}$  is the rotational velocity  $r\Omega$  and  $\mathbf{B}$  is the poloidal field  $r^{-1}\partial(rA_\phi)/\partial r$  for vector potential  $A_\phi = (\psi/2\pi r)$  where  $\psi(r)$  labels “poloidal” magnetic flux surfaces emerging normal to the disk. By transforming from the radial variable  $r$  to  $\psi(r)$  as the coordinate, the voltage difference  $V_{a,b}$  between two radii  $r = a,b$  where a given  $\psi(r)$  intercepts the disk is given by:

$$V_{a,b} = \int_a^b dr [r^{-1} (\partial\psi/\partial r) r\Omega(r)] = \int_a^b d\psi \Omega(\psi) \quad (4)$$

where the frequency  $\Omega(\psi)$  describes Keplerian rotation. For accretion with angular momentum [2], the average radius  $a_o$  representing  $a,b$  can be estimated by equating the rotational energy of an accreted disk mass  $M_D$  to its gravitational energy due to a black hole of mass  $M$ , giving  $1/2 M_D(\Omega a_o)^2 = M_D MG/a_o$  from which we obtain:

$$(\Omega a_o/c) = (R_G/a_o)^{1/2}, \quad R_G = (2MG/c^2) \quad (5)$$

where  $R_G$  is the Schwarzschild radius representative of the event horizon,  $c$  being the speed of light. Eq. (6) is valid if  $(\Omega a_o/c) < 1$ .

In the electrically-conducting environment of the accretion disk,  $V$  causes current to flow along field lines connecting pairs of radii  $a, b$ . As is discussed in Sections 4 and 5, this causes stretching of the field lines if electromagnetic forces on the ions exceed gravity. Stretching the field applies a force to mass injected onto the field lines as current. The current arises wherever this force is first able to eject ion masses in competition with gravitational attraction. This will occur somewhere above the event horizon, at a distance  $d$  from the center of the black hole, allowing ions to escape if  $V > V_G$  given by:

$$V_G = \int_d^\infty dz (m_i MG/z^2 e) \quad (6)$$

where  $m_i$  is the ion mass,  $G$  is the gravitational constant and again  $M$  is the black hole mass at a depth  $d$ , the lower limit of integration. For numbers below and a black hole

mass of  $3 \times 10^{37}$  kg ( $10^{62}$  ergs), Eq. (5) gives  $(\Omega a_0/c) = 0.2$  and, for  $d \approx 0.1 a_0$ , Eq. (6) gives  $V_G = (10^{20}/d) = 10^9 \ll V$ . Details are discussed in Appendix A1.

We first consider the case in which the inner radius  $r = a$  serves as the anode emitting ions. We will find that ions are quickly accelerated to relativistic speeds, giving a density  $\propto$  the current  $I$ , given by:

$$n = (I/e\langle v \rangle A_s) \rightarrow (I/ecA) \quad (7)$$

where  $e$  is the charge,  $\langle v \rangle$  is the average current-carrying speed and  $A_s$  is the surface area, giving the expression on the right as  $\langle v \rangle \rightarrow c$ .

In our model, the minimum density on the right hand side of Eq. (7) is also the density in the central column with radius  $a$  and area  $A = \pi a^2$ . A large influx of colder gas or plasma could increase the density. But there is no likely source to increase the density in the central column of the giant radiolobe structure. Unionized gas feed through the sheath is an unlikely source, since  $\Delta_s \ll a$  for parameters of interest. Feed from accreting mass and ambient pressure outside of the radiolobe is unlikely, since the central column is shielded by the return flux plasma and the magnetic field of the jet/radiolobe structure. Thus we can take Eq. (7) to be the density all along the central column; again, see Appendix A1.

Note that, in dividing by the full area  $A$ , Eq. (7) assumes that the current, and hence the density, are distributed radially across the profile, as would be the case for magnetic relaxation. The local magnitude  $n(r)$  will be important in determining instability conditions in Sections 5 and 6, the lower  $n$  found by dividing by the full area  $A$  generally being the more conservative choice in determining stability boundaries.

#### 4. Evolution of the Magnetic Structure: MHD Simulations

The magnetic structures of Ref. [5] are snapshots of an expansion process in which the column is constrained radially by a striated ambient pressure decreasing away from the disk [5].

The prominent features of the toroidally-averaged field are the central column of current and magnetic flux, and the expanded lobe between the central column and its

return flux confined by the ambient pressure. As noted in Section 2, these are also the characteristic features of spheromak plasmas created by electrostatic gun injection, where a metal wall plays the role of the ambient pressure. In both cases, the configuration is created by expansion of the flux when the current becomes strong enough to stretch and twist the field lines. The main differences are: (a) in the laboratory, the voltage is produced by a capacitor bank; and (b) the small size and relatively long timescale of laboratory experiments often allows complete magnetic relaxation filling in the lobe with current.

Concerning point (a) above, the difference in voltage source has little effect, because magnetic relaxation rather than the voltage source largely determines the geometry of the magnetic field. As noted in Section 2, this follows from the typical timescale whereby the magnetic field given by Eq. (2) is at all times approximately a solution of  $\mathbf{j} \times \mathbf{B} = 0$  with  $\mu_0 \mathbf{j} = \lambda(\psi) \mathbf{B}$  where again  $\psi$  denotes a poloidal flux surface. For complete magnetic relaxation,  $\lambda$  is a constant [9], whereas here there is insufficient time for magnetic relaxation in the radiolobe, giving a very small  $\lambda$  there. However, it is known that, for any  $\lambda$  profile, the toroidally-averaged solutions of  $\mu_0 \mathbf{j} = \lambda(\psi) \mathbf{B}$  give a collimated structure like that shown in Ref. [5]. Also, these force-free solutions have high rigidity, always following the shape of the instantaneous boundary, consistent with the varied shapes observed for giant radiolobes to be expected if intergalactic “winds” distort the ambient pressure boundary confining the magnetic structure [2].

Concerning point (b), the large size and limited duration of the giant radiolobes means that magnetic relaxation is not complete inside the lobe. Instead, the magnetic field in the lobe is essentially the “vacuum” field due to current in the central column. That the lobe field is approximately a vacuum field is confirmed in Ref. [5]. The vacuum field inside the lobe of radius  $R$  contains most of the magnetic energy, a factor  $\ln(R/a)$  more than that inside the central column of radius  $a$ . Thus one would expect the expansion rate  $dL/dt$  of the length  $L$  to decrease like  $1/(\ln R/a)$  as the lobe expands, as shown in Section 5.

Finally, we consider the 3D structure representing current-driven instability – “kink” modes – to be expected for a central column separated from the boundary, even for a current column attached to its source [11], verified in detail for our simulations in

Ref. [12]. It is kink instability that guarantees some acceleration of ions and electrons in expanding magnetic structures, even for plasmas obeying the ideal MHD Ohm's Law given in Eq. (3). While acceleration would surely occur given  $E_{||}$  parallel to the magnetic field, the solution of Eq. (3) gives  $\mathbf{E} \cdot \mathbf{B} = 0$ . Nonetheless, instability produces a toroidally-averaged parallel electric field given by:

$$E_{||} = - \langle \mathbf{v}_1 \times \mathbf{B}_1 \rangle_{||} = - \langle \mathbf{E}_1 \cdot \mathbf{B}_1 / B_o \rangle_{||} \approx v_A B_o (B_1/B_o)^2 \quad (8)$$

where both  $\langle \dots \rangle$  and the subscript o denote a toroidal average and  $\mathbf{B}_1 = \mathbf{B} - \mathbf{B}_o$  describes a tangled magnetic field, and on the far right we introduce  $v_1$  obtained by linearizing Eq. (3). For MHD modes, we take  $E_1/B_o \approx v_A (B_1/B_o)$  with Alfven speed  $v_A$ , giving the expression on the far right hand side. Resistivity or radiative dissipation can extend the unstable domain, yielding “tearing modes” that also contribute to Eq. (8) [13].

Introducing Eq. (8) into the toroidally-averaged momentum equation for ions or electrons (or their toroidally-averaged Vlasov equations) would produce acceleration of the particles. Acceleration acts as an impedance over and above that due to the growing vacuum field in the lobe. The contribution of the central column to this impedance is small if an integral  $ds$  along field lines of length  $L$  gives  $\Delta V \ll V$ , where  $V$  is the disk voltage and  $\Delta V$  is given by:

$$\int ds E_{||} = \Delta V \approx L v_A B_o (B_1/B_o)^2 \quad (9)$$

We will find that  $\Delta V \ll V$ , indicating that the central column transports energy to the nose almost undiminished, as noted in Section 2.

## 5. Evolution of the Magnetic Structure: Theoretical Model

To extrapolate the MHD simulations of Section 4 to astrophysical objects, we will use a simple circuit model of current injection that explains spheromaks in the laboratory [10]. The theoretical basis for this model is limited magnetic relaxation, discussed in Appendix A2, whereby we know the spatial distribution of the poloidal magnetic field and the poloidal current inside the central column and return flux. Then the field and

current can be described by two lumped circuit parameters, the voltage  $V$  representing rotation with total “poloidal” flux  $\psi$  normal to the disk, and the current  $I$  giving the twist or “toroidal” component of the flux. The plasma processes causing magnetic relaxation, including Eq. (8), are discussed in Appendix A3. These processes also serve to allow the penetration of the inductive electric field inside the otherwise perfectly-conducting plasma carrying the current, as electron-ion collisions (negligible here) do in the laboratory.

Given magnetic relaxation inside the central column but not in the lobe, the magnetic energy stored in a giant radiolobe of length  $L$  and radius  $R$  is described by:

$$\int d\mathbf{x} (B^2/2\mu_o) = 1/2 (L_1 I^2); \quad L_1 = (\mu_o/2\pi)L \ln R/a \quad (10)$$

Here the integration is over the upper half of the volume of the structure in Fig. 1A, bounded above by the last closed flux surface and bounded below by a plane cut through the disk. In the inductance  $L_1$  the factor  $\ln R/a$ , mentioned in Section 2, accounts for magnetic energy inside the radiolobe due to the current  $I$  in the central column of radius  $a$  (for cgs units, substitute  $\mu_o \rightarrow 4\pi/c$ ). The total power going into the evolving structure, derived in Appendix A2, is:

$$IV = d/dt \{1/2 (L_1 I^2)\} + \int d\mathbf{x} \mathbf{j} \cdot \mathbf{E} \quad (11)$$

The time derivative has two contributions, one due to changes in the volume that is dominated by the magnetic term for the minimum density in Eq. (7), and one due to changes within the volume. The kinetic contribution to the latter comes from the acceleration of particles, which we represent as:

$$\int d\mathbf{x} \mathbf{j} \cdot \mathbf{E} = \langle \alpha \rangle IV \quad (12)$$

We substitute Eq. (12) into Eq. (11) with the scaling parameter  $\langle \alpha \rangle = 0.5$  justified below.

This gives:

$$IV = 2[d/dt (1/2 L_I I^2)] \quad (13)$$

Relating Eq. (13) to accretion disk parameters requires expressing  $V$  and  $I$  in terms of the average disk rotation frequency  $\Omega$ , poloidal field  $B_o$  and the representative radius  $a_o$ , giving a poloidal flux  $\psi = \pi a_o^2 B_o$ . We approximate the voltage in Eq. (4) by:

$$V = (\Omega\psi/\pi) = \Omega a_o^2 B_o \quad (14)$$

As is discussed in Appendix A2, as  $V$  and  $I$  grow during accretion, at first an equilibrium can exist with magnetic fields confined to the neighborhood of the disk. Wind-out of the flux begins only when  $I$  increases to the point that the toroidal field due to  $I$  becomes comparable to the poloidal field at the disk, giving  $B_{TOR} = (\mu_o I / 2\pi a_o) = B_{POL} = (\psi / \pi a_o^2)$  from which:

$$I = (2\psi / \mu_o a_o) = (2\pi a_o B_o / \mu_o) \quad (15)$$

For the density in Eq. (7), we will find that the Alfven speed is of the order of  $c$ . Hence inductance rather than inertia limits the wind-out rate, giving a current that is always near the threshold value in Eq. (15), as shown in Appendix A2. Also, most of the energy transfer to the giant radiolobe occurs when  $a_o$  is less than twice its final value during the life of the radiolobe. Thus during the wind-out we can take  $I \propto a_o B_o \propto \psi / a_o$  to be constant, given by Eq. (15). Setting the current equal to that in Eq. (15) serves as the boundary condition representing the electrostatic sheath discussed in Section 3.

For constant current, and ignoring  $(L/R)(dR/dt)$  compared to  $(\ln(R/a))(dL/dt)$ , Eq. (13) gives, using Eqs. (14) and (15) :

$$dL/dt = (\Omega a_o / X) \quad (16)$$

$$X = 2[1/2 \ln(R/a)] = \ln R/a \quad (17)$$

where typically  $X \approx 20$  for giant radiolobes. A similar result is given in Ref. [7] but without the factor  $\ln R/a$ . Eq. (16) follows from helicity conservation alone, as discussed in Appendix A2.

To relate the central column radius  $a$  to  $a_o$  in the disk, we note that, for the relatively slow flux expansion according to Eq. (16), we can assume a quasi-steady state all along the central column, giving as the force balance, Eq. (2):

$$-\partial/\partial r [(B_{\text{TOR}}^2 + B_{\text{POL}}^2)/2\mu_o] = \partial/\partial r [(nm_i\gamma_i v_\perp^2)] \quad (18)$$

where the left hand side is  $\mathbf{j} \times \mathbf{B}$  of Eq. (2) neglecting cylinder effects and the right hand side is an approximation to the pressure tensor term of Eq. (2) with  $\mathbf{P} = \nabla \cdot \int d\mathbf{p} \mathbf{p} \mathbf{v} f_o$  for a momentum distribution  $f_o$  due to acceleration of the ions with energy  $\gamma_i$  in rest mass units and velocity component  $v_\perp$  along the radial pressure gradient. As  $v_\perp \rightarrow c$ , an omitted centrifugal force term in  $\mathbf{P}$  is of the same order as that given above. For simplicity, here and hereafter we treat a single species of ions, which we take to be protons, representative of extragalactic cosmic rays [1,3].

We integrate Eq. (18) with radial boundary conditions  $B_{\text{TOR}} = 0$  at  $r = 0$  and  $n = B_{\text{POL}} = 0$  at  $r = a$ , and we divide by  $B_{\text{POL}}^2/2\mu_o$ , giving:

$$[1 - (B_{\text{POL}}^2/B_{\text{TOR}}^2)] = \beta \equiv 2\mu_o(nm_i\gamma_i v_\perp^2)/B_{\text{TOR}}^2 \quad (19)$$

We must also match boundary conditions at the disk, giving a toroidally-averaged poloidal current and flux equal to those in the disk, hence  $B_{\text{POL}} = \psi/\pi a^2$  on axis and  $B_{\text{TOR}} = (\mu_o I/2\pi a)$  at  $r = a$ . Only  $B_{\text{POL}}$  and  $n$  on axis are dependent on details of the current profile. Substituting these values for the field components and  $n = (I/ecA)$  from Eq. (7), we obtain:

$$(1 - a_o^2/a^2) = \beta = (a_o/a)\{4(r_{\text{Lo}}/a_o)(v_\perp/c)^2\} \quad (20)$$



where  $r_{Lo} = (m\gamma c/eB_{TOR})$  for ions. A force-free solution with  $\beta \ll 1$  obtains if the quantity  $\{\dots\} \ll 1$ , as is true for central column parameters derived in Section 7. Then pressure balance requires  $B_{POL} = B_{TOR}$  (a force-free field), giving  $a = (2\psi/\mu_o I) = a_o$  by Eq. (15), hence also  $B = (\mu_o I / 2\pi a) = (\mu_o I / 2\pi a_o) = B_o$ . That is, the toroidally-averaged central column is a straight cylinder having the same radius and magnetic field as the disk:

$$a = a_o, \quad B = B_o \quad \text{central column} \quad (21)$$

Similar considerations apply as ions leave the central column and enter the radial portion of the return flux at the top of Fig. 1A. Now the toroidal field in Eq. (19) is found by integrating  $\nabla \times \mathbf{B} = \mu_o \mathbf{j}$  across the flux return to obtain  $B_{TOR} = (\mu_o I / 2\pi r)$ , while  $B_{POL} = \psi/A$  with area  $A \rightarrow 4\pi r \Delta$  for a flux channel half-width  $\Delta$ ; and we still assume that ions carry the current, giving the density in Eq. (7). We obtain:

$$[1 - (a_o/4\Delta)^2] = \beta = (r_L/\Delta)(v_\perp/\langle v \rangle) = (a_o/4\Delta)\{4(r_{Lo}/a_o)(v_\perp^2/c\langle v \rangle)\} \quad (22)$$

where we now allow  $\langle v \rangle < c$  as discussed in Section 7. In the middle expression we introduce the actual Larmor radius  $r_L = (m\gamma v_\perp/eB_{TOR}) = r_{Lo}(v_\perp/c)$  where  $\gamma$  and  $v_\perp$  giving the pressure are to be understood as values averaged over the distribution function  $f_o$ .

It follows from Eqs. (16) and (21) that the observed length  $L$  and estimated lifetime  $\tau$  for giant radiolobes yield the disk rotational velocity, giving, with  $dL/dt = L/\tau$ :

$$\Omega a_o = (LX/\tau) \leq c \quad (23)$$

Also, we assume for our model that the maximum cosmic ray energy  $E_{CR} = \alpha eV$ , where  $\alpha$  represents the maximum utilization of  $V$  to accelerate ions, as compared with the average value taken as  $\langle \alpha \rangle \approx 1/2$  in Eq. (12). Then Eqs. (14) and (15) give the voltage  $V$  in terms of the current  $I$  and disk parameters, and from this the injection energy  $E_{INJ}$ :

$$V = (\Omega a_o)(a_o B_o) = (\Omega a_o)(\mu_o I / 2\pi) = (E_{CR}/\alpha e) \quad (24)$$

$$E_{\text{INJ}} = \tau IV = \tau (2\pi/\mu_0 \Omega a_0) (E_{\text{CR}}/\alpha e)^2 \quad (25)$$

Substituting into Eqs. (23) and (24) typical values from Ref. [2] ( $L = 10^{22} \text{ m}$ ,  $\tau = 10^8 \text{ yrs} = 3 \times 10^{15}$ ,  $E_{\text{CR}} = 2 \times 10^{19} \text{ electron volts}$ ), and anticipating  $\alpha = 0.7$  and  $X \approx \ln R/a \approx 20$  with  $a = a_0$  by Eq. (21), we obtain:

$$\Omega a_0 = 0.2 \text{ c} ; \quad (a_0 B_0) = 5 \times 10^{11} \quad (26)$$

The numbers in Eq. (26) determine  $V = 3 \times 10^{19} \text{ volts}$  by Eqs. (14) and (24) and  $I = 2.5 \times 10^{18} \text{ amps}$  by Eq. (15) and hence the injected energy  $E_{\text{INJ}} = 2 \times 10^{53} \text{ joules} = 2 \times 10^{60} \text{ ergs}$  by Eq. (25). This is about 10% of the black hole rest mass energy, as derived from the approximate Eq. (5) giving a Schwarzschild radius  $R_G = 4 \times 10^{10} \text{ m}$ , hence a black hole rest mass  $M = 3 \times 10^{37} \text{ kg}$  equal to  $2 \times 10^{54} \text{ J} = 2 \times 10^{61} \text{ ergs}$ .

## 6. Electron Synchrotron Radiation

Additional information comes from electron synchrotron radiation. The rate of energy loss by synchrotron radiation for charged particles following curved orbital paths with rotation frequency  $\omega_r$  is given by [14]:

$$P_{\text{RAD}} = (e^2 \gamma^4 \omega_r^2 / 6\pi \epsilon_0 c) \quad (27)$$

In Appendix A5 we argue that plasma turbulence occurring at parameters of the central column would scatter electrons, giving a synchrotron radiation rate obtained by substituting  $v_c = v_\perp = c$ ,  $\omega_r = (c/R_c)$  and  $R_c = r_{Le} = (cm\gamma/eB)$  into Eq. (27) [14, 15]:

$$P_{\text{RAD}} = (e^4 \gamma_e^2 B^2 / 6\pi \epsilon_0 m_e^2 c) \quad (28)$$

in watts per electron. For electron synchrotron radiation, the observed frequency  $\omega = kc = \gamma_e^3 (eB/m_e \gamma_e)$  [14]. Let  $k = (2\pi/\lambda_s)$  for the observed wavelength  $\lambda_s$  for the lowest harmonic. For  $\lambda_s$  in cm (but  $B$  in MKS), this gives:

$$\gamma_e^2 B = 1/\lambda_s ; \quad B \leq 1/\lambda_s \quad (29)$$

where the inequality follows from  $\gamma_e \geq 1$ .

We calculate the radiated power by multiplying Eq. (28) by the total number of electrons in the central column, and we set this equal to the input power. Note that, aside from the anode sheath, the voltage drop along a 2D central column expanding at constant radius would be essentially zero. As discussed in Section 5, an actual voltage drop  $\Delta V$  must arise from 3D magnetic instability of the central column, producing an effective impedance in 2D, as discussed in Appendix A3. Assuming some  $\Delta V$ , and using  $n$  from Eq. (7), we obtain:

$$I \Delta V = (L A n) (e^4 \gamma_e^2 B^2 / 6 \pi \epsilon_0 m_e^2 c) = I L K (B / \lambda_s) \quad (30)$$

On the right hand side, we use Eqs. (7) and (29) and we took  $B = B_0$  by Eq. (21). The constant  $K = (e^3 / 6 \pi \epsilon_0 m_e^2 c^2) = 3.4 \times 10^{-4}$ . Canceling  $I$ 's gives a formula for  $\Delta V$  in terms of the disk field  $B_0$ :

$$\Delta V = L (K / \lambda_s) B_0 \leq L (K / \lambda_s^2) \quad (31)$$

where Eq. (29) gives the inequality on the right.

The wavelength  $\lambda_s$  in Eq. (31) is meant to be that at the peak of the synchrotron power spectrum for radiation at an average magnetic field  $B_0$ , whereas electrons at a given temperature produce a broad spectrum below the peak [14], and a “runaway tail” would produce a decreasing power spectrum above the peak [15]. As an example, here we take  $\lambda_s = 2$  cm as representative of a massive black hole. For the typical parameters listed above (giving Eq. (26)), and taking  $eV = (E_{CR}/\alpha) = (E_{CR}/0.7)$  and  $\lambda_s = 2$  cm, we find  $\Delta V/V \leq 0.03$ , corresponding to a magnetic fluctuation amplitude  $B_1/B_0$  of order  $10^{-6}$  by Eq. (9), in agreement with calculations in Appendix A6.

Using Eq. (26) and also Eqs. (29) and (30) (with the equalities), we obtain:

$$B_o = 0.5 \text{ tesla}, \quad a_o = 10^{12} \text{ m}, \quad (\Omega a_o) = 0.2c, \quad \Delta V/V = 0.03 \quad (32)$$

This  $a_o$  gives  $X = 20$  as assumed, with typical  $R \approx 1/3 L$ , and an anticipated value  $\alpha = 0.7$  discussed in Section 8. The quantity  $\Delta V/V$  is the fraction of the power going into electron synchrotron radiation along the central column. Keeping the inequalities would give even smaller  $\Delta V/V$ . It is the small value of  $\Delta V$  that justifies the “vacuum” field calculation of the inductance factor  $X$  in Eq. (17). Taking the equality in Eq. (29) gives  $\gamma_e \approx 1$  in the central column and  $B = 1/\lambda_s$ .

The active disk radius  $a_o = 10^{12} \text{ m}$  in Eq. (32) is consistent with expectations [2,3] and helps to justify our assumption of a low density  $n = (I/ecA)$  in Eq. (7) used in Eq. (30) to determine  $\Delta V$  giving rise to electron synchrotron radiation, and in Eq. (20) giving the low plasma  $\beta$  indicating a force free field in the central column. An  $n$  five orders of magnitude larger still gives  $\beta \ll 1$  while a 100-fold increase in  $n$  would give an impossible  $\Delta V > V$ . Further justification for  $n = (I/ecA)$  giving the above results is given in Appendix A1.

The above model of electron synchrotron radiation differs markedly from that in Ref. [15], in which radiation occurs in the weak magnetic field inside the radiolobe. In our model, the observed synchrotron radiation comes mainly from the 2D projection of the magnetic field giving the pronounced central column of figures in Ref. [5]. Even so, synchrotron radiation can appear to arise throughout the radiolobe due to the kink instability that winds up the central column inside the radiolobe, as shown in Fig. 1B. For the numbers above,  $c\tau \approx 100 L$  giving at most  $100/\pi = 30$  turns inside the lobe, similar to results in Ref. [5].

## 7. Quasi-Steady Ion Acceleration

Violent transient events [3] and coherent plasma waves acting as accelerators [3A, 8] have been proposed to account for ultra high energy cosmic ray ions. While such phenomena may occur, in this Section we show that cosmic rays can largely be accounted for by a straight-forward extrapolation of the steady turbulence-driven acceleration model

that was shown to fit electron synchrotron data in Section 7. Large transient events suggested in Ref. [3] are discussed in Section 9.

As in Section 3, we first assume that the center of the disk serves as an anode ejecting ions into the central column. The voltage drop  $\Delta V$  due to kink instability would also accelerate ions in the central column, limited by ion synchrotron radiation. Though we do not expect ions to be scattered as readily as electrons, ions with speed  $v_c$  parallel to  $\mathbf{B}$  do radiate in following curved field lines, by rotation at a frequency  $\omega_r = (v_c/R_C)$  where  $R_C$  is the radius of curvature. Using this frequency in the synchrotron radiation power per ion in Eq. (27) gives for the ion energy  $\epsilon_i$ :

$$d\epsilon_i/ds = e[E_{||} - (P_{\text{RAD}}/ec)] = e[E_{||} - (e/6\pi\epsilon_0)(\gamma^4/R_C^2)] \quad (33)$$

where  $s$  the length along field lines. Dividing by  $m_i c^2$  giving  $\gamma = (\epsilon_i/m_i c^2)$ , we obtain for protons:

$$d\gamma/ds = 10^{-9}[E_{||} - 10^{-9}(\gamma^4/R_C^2)] \quad (34)$$

We first apply Eq. (34) to the central column with  $R_C = a_0$  and constant  $E_{||}$ . Integrating gives approximately:

$$\gamma = 10^{-9} s E_{||} < 2 \times 10^8 E_{||}^{1/4} \text{ acceleration} \quad (35)$$

where the maximum value on the right is that which makes  $d\gamma/ds = 0$  by Eq. (34), using  $a_0 = 10^{12}$  from Section 7. Solving for  $E_{||}$  gives as the condition for acceleration:

$$E_{||} < (10^{23}/s^{4/3}) \quad , \quad \gamma = (se E_{||}/m_i c^2) < (10^{19}/s^{1/3}) \quad (36)$$

For quasi-steady acceleration along the length  $s = L = 10^{22}$ , this gives  $\gamma \approx 10^7$ , more precisely  $\gamma = 2 \times 10^7$  for the exact maximum value. In Appendix A4, we draw similar conclusions even if the current breaks up into force-free filaments as discussed in Ref. [3]. Thus we conclude that the highest  $\gamma$ 's achievable by quasi-steady acceleration in the

central column are order  $\gamma = 10^7$  corresponding to a proton energy of  $10^{16}$  eV. This gives a Larmor radius  $\ll a_0$  as is required for our force-free model of the central column, but this energy is more than a 1000 times below that required to explain ultra energetic cosmic rays.

Higher ion acceleration energies not limited by synchrotron radiation can be achieved after ions enter the nose where the magnetic field begins to fall  $\propto 1/r$ . Since the magnetic free energy driving turbulence also decreases rapidly, we postulate that turbulence levels in the near nose region are actually those generated in the central column, with a radial extent of order  $R^*$  given by:

$$R^* = (\mu_0 I / 2\pi B_1) = a_0 (B_o / B_1) \quad (37)$$

Then the electric field analogous to Eq. (8) would be, with local field  $B = B_o(a_0/r)$ :

$$E_{||} = cB(B_1/B)^2 = cB_o(B_1/B_o)^2(r/a_0) = (E_{||})_{cc}(r/a_0) \quad (38)$$

where  $(E_{||})_{cc}$  is the value in the central column for a given fluctuation level. Introducing Eq. (38) into Eq. (34) and solving for  $(E_{||})_{cc}$  gives acceleration over a range  $r < R^*$  in the nose not limited by synchrotron radiation if the following is satisfied:

$$(E_{||})_{cc} < [3 \times 10^7 / (r/a_0)^{5/3}] \quad \text{acceleration in the nose} \quad (39)$$

Condition Eq. (39) is well satisfied for quasi-steady acceleration with  $(E_{||})_{cc} = 1.5 \times 10^{-4}$  found in Section 6, giving a wide margin of validity up to  $r < 5 \times 10^6 a_0$ , which will prove adequate, as discussed below.

Though we conclude that quasi-steady acceleration should occur in the nose, this regime continuing kink mode acceleration into the nose cannot long persist. Since  $B \approx B_{TOR}$  decreases as  $1/r$  (from Section 5), finally the ion Larmor radius  $r_L \rightarrow \Delta$ . At  $r = b$  where  $r_L \rightarrow \Delta$  all energetic ions might escape. We postulate that, instead, the magnetic field begins to increase  $\Delta$  in order to contain the ions, as it would if  $\beta = (r_L/\Delta)(v_{\perp}/\langle v \rangle) \rightarrow 1$  in Eq (22). While  $r_L = \Delta$  is not sufficient to guarantee  $\beta \rightarrow 1$  for the minimum  $v_{\perp}$  to

confine ions to field lines, escape would increase  $v_{\perp}$  enough to do this. At  $\beta \rightarrow 1$ ,  $B_{\text{POL}}/B_{\text{TOR}} \ll 1$  by Eq. (22), which implies that the flux half-width  $\Delta$  has increased giving a much weaker poloidal field at fixed poloidal flux. Then orbital motion is primarily perpendicular to  $B_{\text{TOR}}$  giving  $v_{\perp} \rightarrow c$  and  $r_L = \Delta$  as  $\Delta$  expands, yielding for relativistic ions:

$$\Delta = \langle r_L \rangle = (\langle E \rangle / ec B_{\text{TOR}}) = r(\langle E \rangle / eV)(\Omega a_o / c) \quad (40)$$

where  $\langle E \rangle$  is the average ion energy and on the far right we use Eq. (14). A similar result was obtained in Ref. [9]. Eq. (40) is correct only for numbers giving  $\Delta \geq a_o$ .

To calculate acceleration in this  $\beta = 1$  regime, we first note that, for  $B_{\text{POL}}/B_{\text{TOR}} \ll 1$ , field lines become longer than  $c\tau$ , in which case acceleration parallel to  $\mathbf{B}$  is no longer viable. Acceleration continues only if some process allows acceleration perpendicular to  $\mathbf{B}$  due to the poloidal electric field produced by  $dL/dt$  expansion, given by solving the ideal Ohm's Law, Eq. (3), to obtain:

$$E_{\text{POL}} = (dL/dt \sin\theta) B_{\text{TOR}} = \sin\theta (V/Xr) \quad (41)$$

where  $\theta$  is the angle between the field line and the axis of symmetry. To obtain the term on the far right, we used  $dL/dt = \Omega a_o / X$  by Eq. (16) and  $B_{\text{TOR}} = (\mu_o I / 2\pi r) = (a_o B_o / r)$  by Eq. (15) to obtain  $V = (\Omega a_o)(a_o B_o)$  by Eq. (14). Eq. (41) gives the poloidal electric field at the advancing flux return of the structure. Integrating along  $dl = dr/\sin\theta$  parallel to poloidal field lines gives:

$$\int dl E_{\text{POL}} = \int_a^r dr (\sin\theta)^{-1} [\sin\theta (V/Xr)] = V (\ln (r/a_o) / X) \quad (42)$$

For  $r = R$ , and using  $X \approx \ln R/a_o$ , this gives  $\int ds E_{\text{POL}} \approx V$ , showing that most of the voltage drop appears across the radial flux return.

In the absence of instability, the electric field of Eq. (41) only produces the  $\mathbf{E} \times \mathbf{B}$  drift motion transverse to flux surfaces that causes ions to “stick” to the moving field lines (omitted in our quasi-static pressure balance). The orbital motion is cycloidal, with

orbits circling around a drifting location called the “guiding center.” Radial motion of the guiding centers is required to produce the net radial ion current required for acceleration. Since collisions are negligible, radial current requires some form of turbulent plasma diffusion process to transport the ions.

Among plasma transport processes that exist in a flux return with ion Larmor radii comparable to  $\Delta$ , we call attention to electrostatic drift cyclotron instabilities studied for magnetic mirror fusion experiments with large ion orbits. For these instabilities, discussed in Appendix A7, turbulence resonant with ion cyclotron motion acts like a collision with collision frequency  $\propto \omega_{ci}$ , the relativistic ion cyclotron frequency, giving a diffusion coefficient in the radial direction of order:

$$D_r \approx \omega_{ci} \langle r_L \rangle^2 = c \langle r_L \rangle \quad (43)$$

with average Larmor radius  $\langle r_L \rangle$  from Eq. (40). Eq. (43) happens to scale like so-called Bohm diffusion, but proportional to the ion energy, not the electron temperature. Other plasma waves are discussed in Ref. [9].

Given radial diffusion, the radial current density is  $j_r = en\langle v \rangle$  where:

$$\langle v \rangle = - (D_r / n) (\partial n / \partial r) \approx D_r / r \approx \Omega a_o (\langle E \rangle / eV) \quad (44)$$

for an average ion energy  $\langle E \rangle$ . Here, anticipating that the mean current would flow at less than speed  $c$ , we took the first form of Eq. (7) giving  $n = (I / (e\langle v \rangle A))$  with  $A = (2\pi r)(2\Delta) = 4\pi r \langle r_L \rangle$ , and we took  $\langle E \rangle$  and  $\langle v \rangle$  to have the logarithmic scaling of the voltage drop in Eq. (42), giving finally  $-n^{-1} \partial n / \partial r \approx (1/r)[1 + (2/(\ln r/a_o))] \approx 1/r$ .

Acceleration of ions gives a current density  $en\langle v \rangle$ , unless electrons cancel the current. Thus a crucial assumption is that the drift cyclotron instability can produce a net radial current by transporting ions radially, but not electrons. Arguments in favor of this assumption are discussed in Appendix A7. If these arguments prove to be correct, we would conclude that plausible processes exist to continue ion acceleration beyond  $r = b$  where radial acceleration begins.



That synchrotron radiation does not affect these conclusions can be seen as follows. As before, we calculate the maximum energy allowed by synchrotron radiation and compare this with the acceleration energy  $E(r)$  neglecting radiation, giving:

$$E(r) \approx \int_b^r dr e E_r = [eV \ln (r/b) / X] < (m_i c^2) \gamma_{\text{SYN}} \quad (45)$$

Here  $E_r = (V/Xr)$  in the flux return, from Eq. (41) for field lines mostly radial ( $\sin\theta = 1$ ), and we begin the integration at  $r = b$ , neglecting parallel acceleration to that point. To calculate the synchrotron limit on the far right, we recall that  $(v_\perp/c) = 1$  for this  $\beta = 1$  regime, so that the radiation rate of Eq. (28) applies. To obtain  $\gamma_{\text{SYN}}$ , we use this radiation rate and solve  $ecE_r = P_{\text{RAD}}$  to obtain, for ions:

$$\gamma_{\text{SYN}} = 2 \times 10^5 (V/a_o B_o^2 X)^{1/2} \sqrt{(r/a_o)} \quad (46)$$

Substituting Eq. (46) into Eq. (45) gives a condition for acceleration which, for our parameters, is satisfied for all  $b < r < R$  with  $b$ 's in Table 1 below. Thus, as anticipated, synchrotron radiation is not an impediment to ion acceleration in the nose.

The radius  $r = b$  where drift cyclotron acceleration takes over is determined by prior acceleration by kink modes in the central column and in the nose giving a rest mass energy  $\gamma$ . We find  $b$  by setting  $r_L = \Delta$ :

$$r_L = (mv_\perp \gamma / eB) = (v_\perp / c)^2 r = (mc\gamma / eB_o a_o)^2 r = \Delta = 1/4 a_o \quad (47)$$

where we use results from Section 5 and half-width  $\Delta = \frac{1}{2} (\psi / 2\pi B_r) = \frac{1}{4} a_o$  for  $B_r = B_\phi = B_o(a_o/r)$  in a force free flux return. Here  $\gamma = \gamma_C + (eV/mc^2)(\Delta V_{ab}/V)$  for energy  $\gamma_C$  emerging from the central column and acceleration voltage  $\Delta V_{ab}$  over  $a < r < b$  in the nose. Solving Eq. (47) for  $r = b$  gives, for numbers in Section 7 [ $\gamma_C = 2 \times 10^7$ ,  $(mc\gamma/eB_o a_o) = 6 \times 10^{-12} \gamma$  and  $(eV/mc^2) = 3 \times 10^{10}$ ]:

$$b/R = 0.01 [1 + 1500 (\Delta V_{ab}/V)]^{-2} < 0.01 \quad (48)$$

Neglecting  $\gamma_c$ , the maximum acceleration efficiency  $\alpha$  due to MHD kink and drift cyclotron acceleration in the nose is, for our numbers:

$$\alpha = \Delta V_{ab}/V + [\ln(R/b)/\ln(R/a_o)] = \Delta V_{ab}/V + 0.2 + 0.1 \ln [1 + 1500(\Delta V_{ab}/V)] \quad (49)$$

We estimate  $\Delta V_{ab}$  using  $E_{||} = cB_o(B_1/B_o)^2(r/a_o)$  from Eq. (38), giving:

$$\Delta V_{ab}/V = \int_a^b dr E_{||}/V = (c/a_o \Omega)(R^2/a_o^2)(1/2 b^2/R^2)(B_1/B_o)^2 \quad (50)$$

where we use  $V = a_o^2 \Omega B_o$  from Eq. (14). Combining Eqs. (48) and (50) gives, for numbers in Section 6:

$$\Delta V_{ab}/V = 3.4(B_1/B_o)^{2/5} \quad (51)$$

In Section 6, we found fluctuations in the central column to be of order  $B_1/B_o \approx 10^{-6}$ , limited by synchrotron radiation. Near the nose where synchrotron radiation finally becomes unimportant, fluctuations can grow to limits set by the free energy due to current in the central column, which we estimate as  $B_1/B_o = 10^{-6}$  in the central column in Section 6. Theoretical estimates in Appendix 6 also give  $B_1/B_o = 10^{-6}$  on time average, giving  $\alpha = 0.5$  by Eq. (49). This estimate omits contributions from transient events discussed in Section 9. Also  $\alpha$  in Eq. (49) is fairly insensitive to the exact value of  $B_1/B_o$ , giving  $0.5 < \alpha < 1$  by Eq. (49) for  $10^{-6} < B_1/B_o < 10^{-3}$  as tabulated in Table 1. Thus we conclude that  $\alpha = 0.7$  assumed in Section 5 is justified. All values of  $b/a_o$  in the table satisfy Eq. (39) for  $r < b$ .

Table 1. Values of  $\Delta V_{ab}/V$  vs.  $\delta B/B_o$

$B_1/B_o$	$\Delta V_{ab}/V$	$\alpha$	$b/R$	$b/a_o$
$10^{-6}$	0.01	0.5	$2 \times 10^{-5}$	$7 \times 10^4$
$2.6 \times 10^{-5}$	0.05	0.7	$2 \times 10^{-6}$	5000
$10^{-3}$	0.21	1.0	$10^{-7}$	300

## 8. Quasi-Steady Cosmic Ray Spectrum

In Section 9, we will conclude that the main intensity of ultra high energy cosmic rays comes from quasi-steady acceleration, while transient events contribute to cosmic rays with energies  $> \text{eV}$ . Here we discuss mechanisms for escape of ions quasi-steadily accelerated in the nose. The escape rate determines the energy spectrum of observed cosmic rays.

Some ions would escape simply by being accelerated, if their guiding centers are so near the outer boundary of the flux return that acceleration causes orbital excursions into fields too weak to bend the orbit on a return path. Here we focus on the likely majority of ions that remain confined inside the flux width  $2\Delta$ . An obvious mechanism for the escape of confined ions is diffusion transverse to the flux return by the same instabilities that accelerate the ions. Since ions carry the current in our model, escaping energetic ions must be replaced by cold ions. While in the central column there is no obvious source of cold ions, a ready source in the “nose” is the (ambient gas/plasma being pushed forward by the expanding radiolobe, and the same instabilities that cause energetic ions to escape can transport cold ions inward, by exchanging hot ions for colder ions. Thus we anticipate that ion ejection as cosmic rays begins only when ions accelerated in the central column reach the nose. After that, their energy distribution  $F_o(E, r, z)$  acquires a cold component, varying also with radius  $r$  and axial position  $z$  across the return flux.

Given  $F_o(E, r, z)$ , a formal expression for the cosmic ray spectrum  $F(E)$  is:

$$F(E) = \int_{R(E)}^R dr dA (-D_T \partial^2 F_o / \partial z^2) \approx (I/e) \kappa^* \int_{R(E)}^R dr D_T (f_o(E) / \langle v \rangle \Delta^2) \quad (52)$$

where  $D_T$  is the transverse diffusion coefficient and on the far right we approximate  $F_o = n f_o = (I/e \langle v \rangle A) f_o(E)$  using Eq. (7), and  $(-dA A^{-1} \partial^2 / \partial z^2) \approx \kappa^* / \Delta^2$  with normalization  $\int dE f_o = 1$ ; an adjustable parameter  $\kappa^*$ ; and a lower integration limit  $R(E)$ , which is a function of the ion energy  $E$ , discussed below.

Eq. (52) sums up emissions of cosmic rays at energy  $E$  at all radial positions along the nose from  $r = b$  outward. We neglect any cosmic ray generation at  $r < b$ , where the voltage drop  $\Delta V_{ab} \ll V$ . For  $r > b$ , where drift cyclotron acceleration dominates, the

maximum energy at  $r$  is given by  $E(r) \approx (eV/X) \ln r/b$  in Eq. (45), neglecting the energy of ions arriving at  $r = b$ . Then the smallest radius  $R(E)$  at which ions with energy  $E$  can be emitted, giving the lower integration limit above, is given by:

$$R(E) = b \exp (EX/eV) \rightarrow b \quad \text{at } E = 0 \quad (53)$$

In this regime, acceleration is due to the drift cyclotron mode, discussed in Section 7, with  $\langle v \rangle \approx D_r/r = D_T/r$  by Eqs. (44) and (A26). Also, as is discussed in Appendix A7, the fact that the primary drive for drift cyclotron instability is the peaked energy distribution created by ion acceleration means that saturation of the turbulence is dominated by diffusion downward in energy that could eventually produce a stable  $f_0$  in competition with the transverse escape time  $\Delta^2/D_T$ . This tends to flatten the energy distribution below the maximum acceleration energy  $E(r)$ , giving approximately:

$$f_0 = (1/E(r)) , \quad E \leq E(r) \quad (54)$$

With this distribution, the natural variable in Eq. (52) is  $E(r) = (eV/X) \ln(r/b)$  giving  $dr \rightarrow dE(r) (rX/eV)$  and an upper integration limit  $E(R) = e\alpha V$  and lower limit  $E(R(E)) = E$ . Using  $\langle v \rangle \approx D_T/r$  as discussed above and  $\Delta = r(\langle E \rangle eV)(\Omega a_0/c)$  by Eq. (40), the  $D$ 's and all  $r$ 's cancel in the integrand of Eq. (52). Taking  $\langle E \rangle \propto E(r)$ , this leaves an integral of the form:

$$F(E) \propto \int_E^{e\alpha V} dE(r) (1/E(r)^3) \propto E^{-2} \quad (55)$$

This suggests a power law, exactly predictable for an exact treatment of turbulence. Given the uncertainties of our simplified treatment, we modify Eq. (55) as:

$$F(E) = \kappa(I/Ee)(E/e\alpha V)^{-(\Gamma-1)} \propto E^{-\Gamma} \quad (56)$$

where  $\kappa^*$  and other constant factors have been gathered into one adjustable parameter  $\kappa$ . Measurements give  $\Gamma = 2.7$  over several orders of magnitude for the sum of all sources reaching Earth (see Ref. [1]; also Fig. 1 of Ref. [3] with the notation  $F(E) = dN/dE$ ).

The adjustable parameter  $\kappa^*$  contained in  $\kappa$  represents self-adjustments of transverse gradients of plasma density and temperature to achieve saturation of the turbulence, as discussed in Appendix A7 for drift cyclotron modes. The reasonableness of  $\kappa$  can be tested by calculating the value required to agree with the recently measured ultra-high-energy cosmic ray flux of  $1/\text{km}^2\text{yr}$  for  $E \geq 10^{19}$  eV, all necessarily arriving from outside our galaxy at distances  $< R_S \equiv 500 \text{ Mlyr} = 5 \times 10^{21} \text{ km}$  [1]. The known number of AGN's within 240 Mlyrs is 472 [1]. Let  $N < 472$  be the number with energies sufficient to contribute cosmic rays with  $E > 10^{19}$  eV. If the  $N$  sources are arranged isotropically within the volume  $V = 4\pi/3 R_S^3$ , then emission from one source  $I_i$  is given by:

$$\Sigma_i (I_i / 4\pi r_i^2) \approx N I_i \int dV (V 4\pi r^2)^{-1} = 0.25 N (I_i / R_S^2) = (1/\text{km}^2\text{yr}) \quad (57)$$

$$I_i = (100/N) \times 10^{42}/\text{yr} \quad \text{measurement} \quad (58)$$

For comparison, our model source with parameters in Eq. (32) would emit:

$$I_i(\text{model}) = \int_{E1}^{e\alpha V} dE F(E) \approx \kappa (I/e) (0.7/1.7) (e\alpha V/E1)^{1.7} \approx \kappa (15\alpha^{1.7}) \times 10^{44}/\text{yr} \quad (59)$$

with  $E1 = 10^{19}$  eV. Agreement between Eq. (57) and Eq. (59) requires:

$$\kappa = (1/15\alpha^{1.7}N) \quad (60)$$

We can bound  $\kappa$  using power balance, as follows. Again we neglect cosmic ray power generated at  $r < b$ . Then the power and  $\kappa$  are bounded by:

$$P = \int_{E^*}^{e\alpha V} dE E F(E) = \alpha IV \kappa \{[(e\alpha V/E^*)^{(\Gamma-2)} - 1]/(\Gamma-2)\}_{DC} \leq \alpha IV \quad (61)$$

$$\kappa \leq (\Gamma - 2) [(e\alpha V/E^*)^{(\Gamma-2)} - 1]^{-1} \quad (62)$$

with  $F(E)$  for  $r > b$  given in Eq. (56). While cold ions are generated by recycle with the ambient, the dominance at  $r > b$  of drift cyclotron modes that would be quenched by very cold ions suggests a lower energy cutoff  $E^*$ , and indeed  $E^* = 0$  gives infinite power. Two likely choices reflecting acceleration prior to  $r = b$  are  $E^*$  at  $\gamma = 2 \times 10^7$  representing ions emerging from the central column, from Section 7; or  $E^* = e\Delta V_{ab}$  representing acceleration over  $a < r < b$ . Using Eq. (62),  $\gamma = 2 \times 10^7$  gives a maximum  $\kappa = 0.005$  giving  $N = 20$  by Eq. (60) (about 5% of the known sources). Taking  $E^* = e\Delta V_{ab} = 0.05$  eV (giving  $\alpha = 0.7$  by Eq. (49)), we find  $\kappa = 0.04$  and  $N = 3$ . Actually calculating  $\kappa$  would require kinetic simulation of drift cyclotron turbulence.

Finally, we note that the above analysis concerns the giant radiolobe as a quasi-steady accelerator, accounting for most of the intensity of cosmic rays at energies  $< eV$  where as before  $V$  is the disk voltage. As is explained in Appendix A6, large but brief transient events in 3D that divert current out of the 2D central column can accelerate some ions to energies  $\gg eV$ .

### 9. Ion Acceleration by Transient Events: Ultra Ultra High Energies

Transient kink modes discussed in Appendix 6 could yield much higher values of magnetic perturbations  $B_1$ , giving much stronger electric fields. Suppose a coherent kink mode with current  $\Delta I$  occurs over an interval  $\Delta s$  along the central column. The current  $\Delta I$  is a 3D twisted column, leaving behind only a current  $I_C = I - \Delta I$  flowing in the 2D symmetrized central column in the interval  $\Delta s$ . The current  $I_C$  could drive smaller random fluctuations  $B_1$  producing tangled fields, yielding an accelerating electric field given by, in analogy with Eq. (8):

$$E_{||} = cB_C(B_1/B_C)^2 = cB_o(B_1/B_o)^2(B_o/B_c) \quad (63)$$

where  $B_C$  is the poloidal field due to  $I_C$ . Ramping down  $B_C$  during a kink event also gives an inductive acceleration -  $(\mu_o/\pi)dI_C/dt$  somewhat higher than Eq. (63) in some parameter regimes. In Appendix 6, we show that  $B_C = B_o(I_C/I)$  and based on free energy

the perturbations are of order  $(B_1/B_o)^2 = (B_1/B(0))^2(B(0)/B_o)^2 = (a_o/ct)$ . It is this estimate that gives, for quasi-steady acceleration corresponding to  $t = \tau$  and  $I_c = I$ , the value  $B_1/B_o = 10^{-6}$  shown to fit electron synchrotron data in Section 7. Introducing this  $(B_1/B_o)^2$  into Eq. (63) gives for the transiently-driven electric field in the central column:

$$(E_{||})_{cc} = cB_o(a_o/ct) (I/I_c) \quad (64)$$

where  $t$  is the duration of  $B_1$  at peak amplitude.

The electric field in Eq. (64) can be much higher than the quasi-steady value of  $1.5 \times 10^4$  volt/m for numbers in Section 6 that we found for quasi-steady acceleration in Section 7. Since synchrotron radiation dominates for a field too large, again radiation dominates acceleration in a transient kink in the central column. Even so the larger  $E_{||}$  gives a much higher limit on  $\gamma > 10^{10}$ , comparable to energies achieved by quasi-steady drift cyclotron acceleration in Section 7. A transiently-accelerated ion observed as a cosmic ray must arise within a distance  $\Delta s$  from the end of the central column, acceleration having occurred in the interval  $L - \Delta s < z < L$ . An ion accelerated further back loses its energy in flowing toward to the nose. The reason for this is that, though in the central column the forward flow of ions is guided by the central column field even if its ion orbit extends into the vacuum field, these ions rapidly lose energy by synchrotron radiation. For example, for an ion that does fit within the column radius, the loss of energy of an ion with an initial  $\gamma = \gamma_o$  traveling a distance  $s$  is found by integrating Eq. (34) for  $E_{||} = 0$ , yielding:

$$\gamma = \gamma_o [1 + (\gamma_o^3/\gamma_1^3)]^{-1/3} < \gamma_1 = 10^6 (R_c^2/3s)^{1/3} \quad (65)$$

In the central column  $\gamma_1 = 3 \times 10^6$  with  $R_c = a_o = 10^{12}$  and  $s = L = 10^{22}$ . Thus we conclude that very large transient-accelerated values of  $\gamma$  are generated at the nose-end of the central column, within a range  $L - \Delta s < z < L$ , after which they escape on entering the nose.

Transiently accelerated particle energies overlap and extend the cosmic ray spectrum. However, the transient intensity would be much less, leaving the quasi-steady

spectrum as the dominant contribution in its accessible energy range. The reason for this is that a transient event uses up locally available energy previously stored in the vacuum field. A second event must await restoration of this energy at a rate  $dL/dt$  and also the time required for growth of new kink modes, though this is probably faster than  $dL/dt$ . The resulting duty cycle is of order  $(t\Delta s^{-1} dL/dt) = (c^{-1}dL/dt) = 1\%$ . Thus we might expect the transient cosmic ray intensity to be  $< 1\%$  of the quasi-steady intensity.

Finally, transient events occurring in the nose itself could yield much higher energies. Again synchrotron radiation dominates, but  $(E_{||})_{CC}$  is amplified by  $(r/a_0)$  as in Eq. (38). Adding this factor, substituting in Eq (33) and setting the right hand side zero gives the maximum radiation-limited acceleration energy:

$$\gamma_i = [(6\pi\epsilon/e)(E_{||})_{CC}(r/a_0)R_C^2]^{1/4} = [10^9(cB_0/\Delta s)(I/I - \Delta I)r^3]^{1/4} \quad (66)$$

where on the right we use Eq. (64) and  $R_C = r$  in the nose, and we estimate  $\Delta s \approx 1/k_z$  for kink wave number  $k_z$  and  $t \approx (k_z v_A)^{-1} = (k_z c)^{-1}$  giving  $\Delta s = ct$ . For our example numbers, even a mild kink in the central column driving fluctuations in an interval  $\Delta s$  in the nose around  $r = b$  could produce energies  $> 10^{21}$  eV, like estimates for coherent wave acceleration in Ref. [4]. Again such events would be limited to a duty cycle  $< 1\%$ .

In Eq. (66), we have assumed that many ions continue to be confined sufficiently to experience  $E_{||}$  even as their Larmor orbit grows beyond  $\Delta$ . A rough criterion, for those mainly making excursions into the vacuum field of the lobe, is, using results from Section 5,  $\Delta s < r_L = (6 \times 10^{-12}\gamma)^2 r$ , which is well satisfied for  $\gamma > 10^{11}$  ( $> 10^{20}$  eV) and  $\Delta s < r < b$  where strong  $\delta B$  fluctuations exist.

## 10. Reverse Polarity, Electron Acceleration, Scaling

Thus far we have assumed that the center of the disk is positive so that ions are injected from the disk into the central column. To our knowledge, the opposite polarity is equally possible and the polarity may be opposite on opposite sides of the disk (quadruple field). With reverse polarity, ions arriving by flow inward from the outer flux return are accelerated inward. For these inward flowing ions, the situation is much the same as our discussions above. Ions are accelerated to an energy  $E(r) = (eV/X) \ln R/r$  yielding  $\beta = 1$



and acceleration and ejection by drift-cyclotron instability, except very near the axis of symmetry. But synchrotron radiation by Eq. (46) dominates at  $r < b^*$  that is comparable to  $b$  for positive polarity.

Electrons are never accelerated to very high energies. As is discussed in Appendix A5, for the parameters of Eq. (32) the two-stream instability that slows down and probably scatters electrons, giving  $v_{\perp} = c$ , occurs everywhere that the force-free solution pertains, and also  $v_{\perp} = c$  for the  $\beta = 1$  regime. Thus Eq. (28) always applies, whereby electron energies are severely limited by synchrotron radiation, with a maximum  $\gamma_e \approx 10^8$  in the flux return. In the weak field at  $r = R$ , the maximum electron energy confined in a force free field is a few GeV, giving  $\gamma_e \approx 10^4$  which happens to agree with observed X-ray emission [3].

Turning to other astrophysical objects that might generate cosmic rays, we first note that, while disk parameters determine the accelerator voltage, the conditions for ion acceleration to the maximum voltage drop  $\alpha V$  are insensitive to disk parameters. The fact that acceleration parallel to  $\mathbf{B}$  persists to about  $0.3V$  ( $\alpha = 0.7$ ), as found in Section 8, depends only the dimensionless ratio  $r/a_0$  aside from a weak logarithmic dependence on the maximum radius  $R/a_0$ . The condition that drift cyclotron instability eventually drives the ion current, thereby allowing acceleration to continue to the energy  $\alpha eV$ , depends only on  $\langle v \rangle / c = \Omega a_0 / c < 1$ .

For a rotation speed approaching  $c$ , the disk voltage  $V$  (giving the maximum cosmic ray energy) and the current  $I$  depend only on the product of the disk radius  $a_0$  and the embedded field  $B_0$ , by Eqs. (14) and (15), giving as the injected power:

$$P = IV = c(a_0 B_0)^2 (\mu_0 \Omega a_0 / 2\pi c) \quad (67)$$

Given also the available energy  $E_{\text{INJ}}$  (a fraction of the black hole mass energy), we then obtain the lifetime  $\tau = (E_{\text{INJ}}/P)$  and the length  $L$  from  $[E_{\text{INJ}} = L\{(\mu_0 X/2\pi)I^2\}]$  by Eqs. (10) and (13)] with  $X = \ln(R/a) \approx \ln(L/3a) \approx 20$  by Eq. (17). The maximum cosmic ray energy is:

$$E_{\text{CR}} = \alpha eV = \alpha e \Omega a_0 (a_0 B_0) \quad (68)$$

For a given black hole mass  $M$ , the representative disk radius  $a_0$  can be crudely estimated by Eq. (6). Similar conclusions apply to rotating neutron stars.

## 11. Conclusions, Future Work

We have arrived at a magnetic model of giant radiolobes that could give rise to the observed synchrotron emission and also ultra-energetic extragalactic cosmic rays reported in Ref. [1]. In contrast with the magnetocentrifugal model much studied in the literature, in our model the observed synchrotron radiation arises from a thin, twisted filament of current inside the radiolobe structure. With adequate resolution to see it, this filamentary structure would provide a distinguishing feature of the model.

In our model, cosmic ray acceleration occurs mainly in the advancing extremity or “nose” where current and magnetic flux expand radially to make their way back to disk. The dominant acceleration mechanism is the inductive electric field due to lengthening of the magnetic structure, producing at the extremity a large radial electric field of order  $(V/Xr)$  where  $X = \ln(R/a) \approx 20$  and  $V = \Omega(a_0^2 B_0)$  with accretion disk spin frequency  $\Omega$ , embedded magnetic field  $B_0$  and representative radius  $a_0$  a few times the Schwarzschild radius. Also, transient events can accelerate a few ions to energies  $\gg eV$ .

Since the inductive field  $\mathbf{E} = -\mathbf{v} \times \mathbf{B}$  has no component parallel to  $\mathbf{B}$ , acceleration requires instability, first producing a toroidally-averaged parallel electric field well known from experiments and MHD simulations, then other instabilities driven by the ion energy that can accelerate ions perpendicular to the toroidally-averaged magnetic field at the extremity where the inductive electric field is highest. Self-consistency is demonstrated by comparing model predictions with observed dimensions and synchrotron radiation wavelengths, giving inferred black hole masses sufficient to produce  $V > 10^{19}$  volts, hence acceleration energies comparable to extragalactic cosmic rays thought to arise from AGN’s. A unique feature of the model is that the cm-range synchrotron radiation and cosmic rays arise from different parts of the structure, as discussed in Sections 6 and 7 of the paper. A simple model yielding the qualitative features of laboratory experiments and our MHD simulations is discussed in Section 5, giving rules to extrapolate from giant radiolobes to other astrophysical objects in Section

10. The acceleration mechanisms mentioned above are explained in Appendices A6 and A7.

While the kink modes giving rise to ion and electron acceleration are contained in MHD simulations, kinetic instabilities giving the acceleration perpendicular to  $\mathbf{B}$  needed to reach the main intensity of ultra high energy cosmic rays require simulations of the Vlasov equation or Particle-in-Cell (PIC) codes at the cutting edge of modern plasma physics. Such calculations are needed to determine the synchrotron and cosmic ray energy spectra to be compared with data as an arbiter of model validity. Approximate cosmic ray spectra discussed in Section 9, and in Ref. [9], suggest that such efforts might be rewarding.

## **Appendix A. Plasma Physics Topics**

This Appendix discusses plasma physics topics referred to in the text.

### **A1. Current Generation, Plasma Density**

This section continues the discussion in Section 3 on the effects of gravity on the creation of current, and the assumption  $n \rightarrow (I/ecA)$  by Eq. (7) that was crucial to our interpretation of electron synchrotron data, as discussed at the end of Section 3.

The importance of gravity follows if current carriers in giant radiolobes arise from the disk itself. This is certainly true for the case discussed in Section 3 in which ion current in the central column emerges from an anode, thus requiring acceleration of the ions to overcome the gravity of the black hole. For the ideal MHD Ohm's Law of Eq. (3), the magnetic field cannot accelerate ion current parallel to  $\mathbf{B}$ . Acceleration requires that an electrostatic sheath form at the anode. An anode sheath is a region of net charge dominated by ions that constitute an ion beam accelerated across the sheath.

In Section 3, we treated the disk center as being analogous to a metallic anode that requires a sheath to create plasma currents completing a circuit with current carried by electrons in the collision-dominated metal. This corresponds to an idealized case of a spinning magnetized disk of defined thickness with rotation frequency  $\Omega(\psi)$  varying radially but independent of  $z$ . Then the radial voltage drop  $V$  given by Eq. (4) would be the same at each  $z$  and the electric field would be purely radial inside the disk. In the

absence of a current, surface charge projects the voltage drop  $V$  onto the disk surface. Magnetic field lines exiting normal to the disk act like “wires” connecting  $r = a$  to  $r = b$  in Eq. (4). If the voltage  $V$  between  $a$  and  $b$  exceeds the escape potential  $V_G = m_i MG/d$  for a black hole of mass  $M$  at a depth  $d$  below the disk surface, ion current flows despite gravity by Eq. (6). The current begins to stretch the field lines, giving a voltage drop  $I(dL_1/dt)$  by Eqs. (10), (13) and (16). But this inductive voltage drop must always adjust to be  $< V$  sufficiently to allow whatever sheath voltage drop  $\Delta\Phi$  is required to maintain a current  $I$  which is in turn self-regulated to equal the value given in Eq. (15), as shown in Appendix A2. The sheath voltage  $\Delta\Phi$  is determined by this dynamics together with Poisson’s equation, as follows.

Consider the scenario of Sections 5 and 6, whereby the system settles to one in which two stream instability in the central column favors ions as the current carrier with speed  $\langle v \rangle$  and limited thermal spread. Then the ion density is  $n_i = (I/eA\langle v \rangle)$ , as in Eq. (7). Beyond the sheath, charge neutrality gives the electron density  $n_e = n_i$ . Thus we neglect electron current and take  $n_e = n_i(\infty)$ , giving a Poisson’s equation of the form:

$$-\nabla_z^2 \phi = \nabla_z^2 \varphi - 2V_G(d/z^3) = (I/\epsilon_0 A)(\langle v \rangle^{-1} - \langle v \rangle_\infty^{-1}), \quad \langle v \rangle = c[(E_i^2 - m_i^2 c^4)^{1/2}/E_i] \quad (A1)$$

On the right hand side, we took  $n_i(\infty) = (I/ec\langle v \rangle_\infty)$  assuming that the ion density in the central column is just that of the ion beam emerging from the sheath, justified in Section 3 by an absence of additional ions injected from the outside due to self-shielding of the central column by the radiolobe itself. On the left hand side, we have changed variables from the electrostatic potential  $\phi$  to the ion potential energy drop  $\varphi = (\Delta\Phi - \phi) - V_G(1 - d/z)$  giving the relativistic ion energy  $E_i = e\varphi + m_i c^2$  used to calculate  $\langle v \rangle$ . In terms of  $\varphi$ , boundary conditions are taken as  $\varphi = 0$  ( $\phi = \Delta\Phi$ ) at  $z = d$  and  $\partial\varphi/\partial z \rightarrow 0$  ( $\partial\phi/\partial z \rightarrow 0$ ) at  $z \rightarrow \infty$ . The usual effect of electrons on  $\Delta\Phi$  in the laboratory [16] is not important here, since, due to synchrotron radiation,  $(T_e/e) \ll V_G$  for numbers in Section 6.

Eq. (A1) assumes an ample supply of ions from the disk and space-charge-limited current emission. Near  $z = d$ ,  $n \propto \langle v \rangle^{-1}$  is singular giving in the non-relativistic limit a Child-Langmuir sheath equation  $\nabla_z^2 \varphi = (\varphi_\infty/\lambda_D^2)(\varphi/\varphi_\infty)^{-1/2}$  with solution  $\varphi = \varphi_\infty [(z -$

$d/\lambda_D]^{4/3}$  [16] where  $\varphi_\infty = (\Delta\Phi - V_G)$  and  $\lambda_D = [e\varphi_\infty/(eI/\epsilon_0 A(2e\varphi_\infty/m_i)^{1/2})]^{1/2}$  (a Debye length at “temperature”  $e\varphi_\infty$ ). To satisfy boundary conditions, this solution joins a constant solution  $\varphi = \varphi_\infty$  at  $z - d \approx \lambda_D$ . This procedure does not determine  $\varphi_\infty$  precisely but it does insure solutions with  $\varphi_\infty = (\Delta\Phi - V_G) > 0$  so that  $\langle v \rangle$  is everywhere positive, thus indicating that the electrostatic sheath alone would force the escape of ions from the black hole if that is required to maintain the current  $I$ . Also, for numbers in Section 7, we found that MHD instability in the central column generates a potential drop  $\Delta V = 0.03V$  that could accelerate protons to speed  $c$  in a distance of order  $10a_0$ . It is this combination of acceleration by  $\Delta\Phi$  and by  $\Delta V$  that leads us to conclude that the density quickly relaxes to  $n = (I/ecA)$  in Eq. (7).

The above discussion assumed that the anode appears at the surface of a disk with well defined thickness, as is the case for a metallic anode bound together by atomic bonds strong enough to overcome electromagnetic forces due to currents flowing radially through the metal (by collisional transport of electrons across magnetic field lines). Now consider the more probable case in which the rotation frequency  $\Omega(\psi, z)$  decreases with increasing  $z$  inside the disk. Then an axial electric field  $E_z$  will exist inside the disk, causing current loops that close inside the disk (again by collisional transport of electrons). At expected values of the resistivity  $\eta$ ,  $\eta j a_0 \ll V$  (also  $V \gg$  the drop from viscosity [7]). Thus these currents would not serve as a resistive short circuit; rather, they would produce stress forces across the disk. While  $\mathbf{j} \times \mathbf{B}$  stress forces inside metallic electrodes usually cannot compete with metallic binding forces, the fact that  $V \gg V_G$  indicates that electromagnetic forces could rupture an accretion disk bound by gravity. The point of rupture defines  $z = d$  where the “anode” is located, as follows.

For a current  $I$  capable of causing a rupture at  $z = d$ , a higher current  $I + \Delta I$  would circulate at  $z < d$  (but above the event horizon) in order to balance higher gravitational stresses there. Where current flows upward, the current loop would branch, with  $\Delta I$  returning radially just below the rupture point and a current  $I$  ejected on magnetic field lines above the rupture. To find the rupture location  $d$  above the black hole, we calculate the force balance near the rupture point giving  $j_r B_\phi \approx [n_D(d)eV_G/d]$  where  $n_D(z)$  is the axial profile of disk density. Substituting  $j_r = (I/a_0 d)$  and  $B_\phi = (\mu_0 I/2\pi a_0)$  gives the following condition relating  $I$  to the density at the point of rupture:

$$n_D(d) = (\mu_0 I^2 / e V_G 2\pi a_0^2) \quad (A2)$$

For numbers in Section 6, Eq. (A2) gives  $n_D(d) \approx 10^{17}(d/a_0) < 10^{17}$ , a low value indicating that disruption can occur only in the low-density coronal edge of the disk. The collisional mean free path at this density is less than the electrostatic sheath thickness so a sheath would form as in the ideal example above. For a diffuse density profile at the time of rupture, ion current initially accelerated out of the sheath would enter field lines already loaded with plasma. At  $n_D(d) < 10^{17}$  the number of ions captured on field lines would be at most only comparable to the the number needed to carry the current at full line length; estimating an average  $\langle n \rangle = 0.1(d/a_0)10^{17} = 10^{15}$  gives  $\langle n \rangle a_0^3 \approx 10^{51} \approx (IL/ec)$ . In any case, the sheath-generated ion current would be sufficient to create instability that would accelerate all ions to speeds  $c \gg dL/dt$  by Eqs. (9) and (16). If so, the original ions would soon flow to the disk, allowing the system to settle down to the ideal solution above.

We must also take into account centrifugal forces as well as gravity. This is not an issue near the axis of symmetry where magnetic field lines emerge perpendicular to the disk, that is, perpendicular to the plane of rotation. However, further out field lines emerge at an angle to the plane, giving finally a centrifugal force due to Keplerian rotation that exceeds gravity for ejection along field lines inclined more than  $30^\circ$  from the axis of symmetry [2,8]. This part of the magnetic flux is embedded inside the flux containing the force free central column to which our sheath model applies, so that our sheath model giving a low density on expanding field lines still describes overall flux expansion and cosmic ray acceleration. That the central column is not much affected by centrifugal effects has been shown even in MHD simulations ignoring electrostatic sheath formation [17]. Moreover, two facts suggest that a sheath may form on all field lines, though the centrifugal force might distort the disruption surface where a sheath forms, Eq. (A2). First, barring a massive injection of pressure from the disk (giving  $\beta = 1$ ), the magnetic field always relaxes to a well-defined quasi-equilibrium as discussed in Appendix A2. Second, if a sheath were needed to supply the necessary current on field lines at angles  $> 30^\circ$ , the sheath electric force would greatly exceed the centrifugal force.

In MHD calculations, the electrostatic sheath must be represented by a boundary condition, as an applied voltage in Ref. [6] or as a flux generator in Ref. [5].

## A2. Helicity Injection

This section discusses the theoretical underpinnings of Section 5 on the magnetic evolution of giant radiolobes, and the self-saturation of the current  $I$  at the value given in Eq. (15).

As noted in the text, we adopt a cylindrical coordinate system in an inertial reference frame centered in the disk, with the axis ( $z$ ) normal to the disk. For any chosen poloidal flux surface  $\psi$  as the boundary, the evolution of a twisted magnetic field with poloidal and toroidal components inside the volume bounded by the chosen flux surface is most precisely described by [18]:

$$dK/dt = 2V\psi - 2 \int d\mathbf{x} \mathbf{E} \cdot \mathbf{B} \quad (\text{A3})$$

where the voltage drop  $V$  across the bounding flux surface is given by Eq. (4) and  $\mathbf{E}$  and  $\mathbf{B}$  are the electric and magnetic fields in our coordinate system and the helicity  $K$  is defined by:

$$K = \int d\mathbf{x} \mathbf{A} \cdot \mathbf{B} \quad (\text{A4})$$

for vector potential  $\mathbf{A}$ . An exact gauge-independent definition of  $K$  is discussed in Ref. [18], valid even for a boundary changing in time as in giant radiolobes. This exact definition can be approximated as  $K \approx \psi\psi_{\text{TOR}}$  where  $\psi$  is the poloidal flux defined in the text and  $\psi_{\text{TOR}}$  is the toroidal flux.

The energy balance Eqs. (11) and (13) in the text follows from Eq. (A3), taking into account magnetic relaxation discussed below. As in Ref. [10], we divide the volume into two parts, the relaxed central cell (and return flux) and the radiolobe where, because of the limited time available, relaxation is incomplete and  $\mathbf{A}$  and  $\mathbf{B}$  are essentially vacuum fields produced by current in the central column; while in the relaxed force-free central column  $\mathbf{B} = \lambda\mathbf{A}$  and  $\mu_0\mathbf{j} = \lambda\mathbf{B}$  with characteristic Taylor relaxation eigenvalue  $\lambda =$

$2/a$  where  $a$  is the central column radius. Multiplying the central column portion of Eq. (A3) by  $(\lambda/2\mu_o)$  gives as the drive  $(\lambda/2\mu_o)(2V\psi) = I_o V$  with  $I_o = (2\psi/a\mu_o)$ , and  $(\lambda/2\mu_o)K = \int dx (B^2/2\mu_o)$  inside the current channel, while the well-specified vacuum field of the radiolobe allows us to extend the volume to include the radiolobe, as in Eq. (10).

In the text, we took as a boundary condition that  $I$  during buildup of the radiolobe saturates near  $I = I_o \equiv (2\psi/a_o\mu_o) = (2\pi a_o B_o / \mu_o)$  by Eq. (15), sometimes called the “bubbleburst” current. The constancy of  $I$  also determines the sheath potential  $\Delta\Phi$  that was not fully determined by Eq. (A1), since  $V$  in Eq. (13) should actually be replaced by  $V - \Delta\Phi - \Delta V$ . The current  $I$  adjusts to Eq. (15); the disk density  $n_d$  at the anode adjusts to Eq. (A2) at this current; and  $\Delta\Phi + \Delta V$  adjusts so as to accelerate ions in the central column sufficiently to keep up with  $dL/dt$ . That  $I$  does saturate at the bubbleburst current can be seen as follows.

Expansion of the column is due to the hoop force implicit in our equilibrium Eq. (2), giving approximately:

$$nm_i dv_z/dt \approx (n/n_o)(j_r/ec)m_i d^2L/dt^2 \approx j_r (\mu_o I/2\pi L) \quad (A5)$$

where  $v_z = dL/dt$  and we allow  $(n/n_o) > 1$  to represent the transient phase of our disruption model of anode formation in Appendix A1, with  $n_o = (j_r/ec)$  by Eq. (7). Also, by Eq. (13), upon differentiating and dividing by  $I$ , we obtain:

$$V = (X\mu_o/2\pi)[I (dL/dt) + 2L (dI/dt)] \quad (A6)$$

where now we ignore  $\Delta\Phi + \Delta V$ , and  $X = \ln(R/a)$  as given in Eq. (17). Eq. (A6) is only valid after bubbleburst,  $I \geq I_o$ . However, as confirmed by numerical solutions of these equations, following a transient during which  $n/n_o \rightarrow 1$  as discussed in Appendix A1, for numbers in Eq. (32) we find that, starting from  $I \approx I_o$ ,  $dL/dt$  grows rapidly by Eq. (A5), which causes  $I$  to fall rapidly below  $I_o$  due to the  $dL/dt$  term in Eq. (A6). Since this is not allowed, actually  $I$  hovers at  $I = I_o$  as in Eq. (15) and  $dL/dt = (2\pi V/XI_o\mu_o) = (\Omega a_o/X)$ , as in Eq. (16). Any actual increase in  $I$  above  $I_o$  would be due to “dissipation” by particle acceleration [9], omitted above but included in Eq. (11).



When a stratified ambient pressure  $p(z)$  is present at height  $z$ , as in Ref. [4], the final radiolobe radius  $R$  is determined by balancing  $p(z) = (B_{\text{TOR}}^2/2\mu_0)$  at the flux return perimeter, as in that reference. At the pressures involved, the length  $L$  probably never reaches equilibrium but instead satisfies Eqs. (A5) and (A6), due to the strong  $\mathbf{j} \times \mathbf{B}$  hoop force in the radial flux return that causes expansion of the length  $L$  to continue until the available energy is exhausted.

We note that the above result, showing that  $L$  continues to expand as long the disk feeds power to the central column, though derived here from energy, actually depends only on helicity conservation discussed in Appendix A of Ref. [10]. We will return to this point in Appendix A6.

### A3. Magnetic Relaxation and Hyper-resistivity

Our model of magnetic field evolution in Section 5 assumes that current is distributed across the central column and flux return. The justification for relaxation is given below. But first we note that the rate of expansion and certain other features of the model depend only on the magnetic energy, which is insensitive to the details of the current distribution. The main reason is that the poloidal current  $I$ , which is fixed by Eq. (15) per the discussion of Appendix A2, is independent of the poloidal current distribution, and the total  $I$  determines the vacuum field inside the lobe that produces most of the magnetic energy as discussed in Sections 2 and 5. Even the energy inside the column only varies a factor of 2 or so ranging from a sheet current (no relaxation) to a distributed current, since most of the energy in the poloidal field is fixed by the boundary condition maintaining constant poloidal flux.

Empirically the rate of magnetic relaxation is given by the observed voltage drops through Eq. (1). For the central column, this gives  $B/t = (\Delta V/La)$  or  $t/\tau = (V/X\Delta V) \approx 1$  for  $X=20$  and  $\Delta V/V = 0.03$ , where we use  $\partial B/\partial t = B_0/t$  and  $\nabla \times \mathbf{E} = \mathbf{E}/a$  and  $E = (\Delta V/L)$  with Eq. (16) for the lifetime  $\tau$  and Eq. (14) for  $B/V$ . Thus the central column is marginally relaxed over a lifetime  $\tau$ . Similarly, relaxation in the nose with  $\nabla \times \mathbf{E} = \mathbf{E}/\Delta$  with  $E = (V/Xr)$  and  $B = (a/r)B_0$  gives  $t/\tau = (\Delta/L) \ll 1$  so relaxation is assured in the nose.

The detailed theoretical justification for relaxation involves the generalized Ohm's Law, as follows. We note that it is the component of  $\mathbf{E}$  parallel to  $\mathbf{B}$  that appears in the helicity injection Eq. (A3), indicating that only  $E_{||}$  can cause helicity to propagate between 2D flux surfaces. This fact has led to keen interest in what is called the generalized Ohm's Law, derived in Ref. [10] from combinations of the momentum moments of the ion and electron Vlasov equations, giving:

$$(ne^2/m_e\gamma_e^3)\langle E_{||} + \mathbf{v}_1 \times \mathbf{B}_1 - E_{\text{RAD}} - \eta_{||} j_{||} \rangle = -\nabla_{\perp} \cdot \Sigma D \nabla_{\perp} q n \mathbf{u}_{||} \quad (\text{A7})$$

The various terms represent departures from the ideal Ohm's Law that allow current to penetrate into the central column and flux return, even though collisional resistivity denoted by the term  $\eta_{||}$  is negligible in giant radiolobes. As mentioned in Appendix A1, collisional resistivity does probably play a role in allowing current to flow across the field lines inside the dense disk where rotation and embedded flux create a  $\mathbf{v} \times \mathbf{B}$  electric field, but resistivity is finite giving rise to the concept of “frozen in” flux [6]. Once distributed in the disk, the current would remain distributed during flux expansion, but not necessarily in the state of magnetic relaxation within the 2D flux channel that we used to reduce flux expansion to a circuit equation above. Synchrotron radiation could promote relaxation in the central column, via the term  $E_{\text{RAD}} = (P_{\text{RAD}}/ec)$ . Plasma turbulence also contributes to magnetic relaxation. Because volume integrations are performed, Eq. (A3) concerns only toroidally-averaged quantities, which however are quadratic and hence involve averages over products of 3D quantities corresponding to turbulence. In Eq. (A7), turbulence appears via  $\mathbf{v}_1$  giving “MHD hyper-resistivity” and turbulence also gives the  $D$  term representing “kinetic hyper-resistivity” due to “micro-instabilities” discussed below. Here  $\perp$  means perpendicular to  $\mathbf{B}_0$ , the toroidally averaged magnetic field, and  $\langle \dots \rangle$  also denotes a toroidal average, while the subscript 1 denotes 3D perturbations. The factor  $(ne^2/m_e\gamma_e^3)$  on the left hand side is large despite our having included a relativistic correction (coming from  $dv/dp = 1/m\gamma^3$ ) that also occurs in the two-stream instability discussed below. This large factor reduces the importance of kinetic hyper-resistivity in the central column, leaving MHD processes as the main mechanism that contributes the 2D inductive voltage  $\Delta V$  in the text [10]. Even ideal MHD kink mode

contributions to  $\langle \mathbf{v}_1 \times \mathbf{B}_1 \rangle$  produce magnetic relaxation of the toroidally-averaged state, with  $v_1 \approx v_A (B_1/B_o)$  for Alfvén speed  $v_A$ , as in Eq. (9). The kinetic hyper-resistivity may play an important role in magnetic relaxation in the flux return where  $D$  is large. Thus there appears to be, for the parameters derived in Section 6, multiple reasons why magnetic relaxation is to be expected.

#### A4. Current Filamentation in the Central Column

Having found in Appendix A2 that inductance rather than inertia determines the rate of expansion of the magnetic structure, we can drop the time derivative in the momentum equation, giving the force balance in Eq. (18) of the text, obtained from:

$$(\mathbf{j} \times \mathbf{B}) = \nabla \cdot \int d\mathbf{p} \, \mathbf{p} v f_o \quad (\text{A8})$$

Dropping cylindrical geometry effects and approximating the pressure term as described in Section 5 gives Eq. (18) for the cylindrical central column of Fig.1A. In Ref. [3], it is pointed out that 3D micro-instabilities can cause the central column to break up into filaments on the scale of the magnetic skin depth  $c/\omega_{pi}$  with ion plasma frequency  $\omega_{pi}$ . For parameters of Eq. (32), this yields  $N_F = 10^{10}$  filaments, each carrying current  $I/N_F$  and poloidal flux  $\psi/N$ . Short wavelength MHD kink modes might also produce filamentation, for say,  $N_F = 10$ . Though unstable, these filaments would nonetheless approximately satisfy Eq. (A8) as they interact with each other, giving a result analogous to Eq. (19). An important difference from Eq. (20) derived from Eq. (19) is the fact that the toroidal field acting on a wandering filament has two contributions, one from the current in the filament and one due to the 2D central column which is the average of all filaments, giving by symmetry a current  $I$  in the force-free central column. Then the toroidal field entering in the force balance for a single filament is:

$$B_{\text{TOR}} = C(\mu_o I / 2\pi r) ; \quad C = [1 + (r/N_F a)] \quad (\text{A9})$$

where  $a$  is the radius of the filament. Using also  $B_{\text{POL}} = (\psi/N_F \pi a^2)$ , we obtain as the filamentary version of Eq. (20):

$$(1 - (a_0 r / N_F Ca^2)^2) = 4(r / N Ca)^2 (N_F K) (v_\perp / c)^2 \quad (A10)$$

where  $(a_0 r / N_F Ca^2) = (B_{POL} / B_{TOR})$  and  $K = (m \gamma c / e a_0 B_o) < 6.4 \times 10^{-3}$  for numbers in Eq. (32) with maximum  $\gamma_i = 10^9$  for  $\Delta V / V = 0.03$ .

That Eq. (A10) yields force-free solutions giving ion acceleration dominated by synchrotron radiation as in the central column, with similar limitations on the maximum ion  $\gamma$ , can be seen as follows. Such solutions require that  $(a_0 r / N_F Ca^2) = 1$  to make the left hand side equal zero. It is straightforward to show that for any  $N_F$  and  $r$  this gives  $a/a_0 \leq \sqrt{3}$ , hence a low synchrotron limit on  $\gamma$  equaling that in the central column, multiplied by  $3^{1/4} = 1.3$ .

One can not so easily eliminate all  $\beta = 1$  solutions analogous to solutions for large  $r$  in the flux return, which require that both sides of Eq. (A10) be about unity simultaneously. More work would be required to reconcile such solutions with residence times in the central columns for wandering filaments that must add up to a net toroidally-averaged current  $I$  in the 2D central column, and also to show that acceleration and ejection mechanisms exist if such filaments are to participate in cosmic ray production. In any case, ion energies would not exceed  $e\Delta V$ , hence well below those in the force-free portion of the flux return, if  $\Delta V / V = 0.03$  as in Eq. (32).

Even if filamentation is unimportant in the central column, it may play a role in ion acceleration in the nose, as discussed at the end of Appendix A6.

### A5. Electron Scattering

The calculation of electron synchrotron radiation in Section 3, giving the results for disk parameters in Eq. (32), assumed that instabilities in the central column scatter electrons giving the radiation rate of Eq. (28). A probable initiating mechanism is the two stream instability occurring between counter-streaming ions and electrons in the central column, with growth rate  $\text{Im } \omega$  given by [16]:

$$\text{Im } \omega = (m_e / m_i)^{1/3} \omega_{pe} (\sqrt{\gamma_e} / \gamma_i) \quad (A11)$$

where we have applied the relativistic correction from Ref. [19]. Eq. (A11) gives  $\text{Im } \omega \tau = 1.4 \times 10^{11}$ , hence strong growth of two stream instability, for numbers in Eq. (32) giving in the central column  $n = 1.8 \times 10^4$  in  $\omega_{pe} = \sqrt{(ne^2/m_e \epsilon_0)} = 7.6 \times 10^3$  and  $\gamma_e \approx 1$  and  $\gamma_i = 1.3 \times 10^7$  due to synchrotron radiation of electrons and ions.

Even in the relativistic case, the two-stream instability is known to spread electron momenta parallel to  $\mathbf{B}$  with little effect on the ions. The result is a highly anisotropic electron pressure distribution with a large free energy to drive instability. Because scattering requires action perpendicular to  $\mathbf{B}$ , the cyclotron frequency is involved, either for electrons acting on themselves [19], or electron plasma oscillations resonant with the ion cyclotron frequency  $\omega_{ci}$  [20]. The low density in the central column gives both  $\omega_{pe} \ll \omega_{ce}$  and  $\omega_{pe} \ll \omega_{ci}$  (for relativistic frequencies), outside the regime most studied in the literature. In any case, PIC or Vlasov simulations would be required to determine the resulting electron energy distribution giving synchrotron spectral distributions that could be compared with observations. The total power given by calculations in Section 7 should not be much affected by the spectral distribution and hence could be compared with available luminosity data [15].

Conditions for two stream instability continue to be satisfied over the force-free portion of the flux return, where the density relative to that in the central column scales as  $n \propto (a_0^2/4\Delta r)$  giving  $\text{Im } \omega \tau = 1.4 \times 10^{11} (1.3 \times 10^7 \sqrt{\gamma_e/\gamma_i})(a_0^2/4\Delta r)^{1/2} > 1$  as the condition for two-stream instability, and electrons transported by diffusion automatically acquire  $v_\perp = c$ . Then electron synchrotron radiation is always given by Eq. (28), giving as the synchrotron-limited energy Eq. (42) (derived for ions) multiplied by  $(m_e/m_i)$ , or  $\gamma_{\text{SYN}} = 55 (V/a_0 B_o^2 X)^{1/2} \sqrt{(r/a_0)}$  which is always less than  $E(r) = (eV/X) \ln R/r$  for electrons with positive polarity, with a maximum equivalent to  $\gamma_e \approx 10^8$  occurring near the central column for positive polarity.

## A6. Transport and Acceleration by Tangled Magnetic Fields

In this Section, we return to the discussion of helicity injection of Appendices A2 and A3, with an emphasis on instability and transport.

Let us first contrast two situations, our disk and a laboratory experiment with a flux conserver of fixed length. Let each be driven by a helicity source at constant current  $I$  with fixed bias flux  $\psi$ . At any instant the helicity per unit length is fixed,  $\propto I\psi$ . For the laboratory experiment, continuous injection of helicity into a column of fixed length produces instability that pumps helicity out of the column into the interior vacuum region of Fig. 1A, causing the magnetic field there to increase until limited by dissipation [9]. Now consider the disk problem. Because the length is growing, pumping in helicity mainly lengthens the column.

That it is helicity alone that drives  $dL/dt$  can be seen using Eq. (A3), giving:

$$\begin{aligned} 2V\psi &= dK/dt = d/dt \int \mathbf{A} \cdot \mathbf{B} \approx d/dt \int_0^R 2\pi r dr (\psi(r)/2\pi r)(\mu_0 I(r)/2\pi r) \\ &\approx d/dt [L(\psi\mu_0 I/2\pi) \ln R/a_0] = dL/dt [(\psi\mu_0 I/2\pi) \ln R/a_0] \end{aligned} \quad (A12)$$

Here we omit the term  $\int \mathbf{E} \cdot \mathbf{B}$  in Eq. (A3), which mainly serves to distribute helicity radially by instability while conserving the total helicity [10], and we retain only the dominant contributions from  $A_\phi$  and  $B_\phi$  evaluated in terms of the cumulative poloidal flux out to radius  $r$  and the cumulative poloidal current  $I(r)$ , found by integrating  $r^{-1}\partial(rA_\phi)/\partial r = B_z$  and  $r^{-1}\partial(rB_\phi)/\partial r = \mu_0 j_z$ , respectively. In the second line, we use the conservation of helicity to write  $K$  as the unperturbed value in the absence of instability, approximated on the right by the constant flux  $\psi$  and current  $I$  tied to disk parameters. Then only  $L$  changes, giving Eq. (16) of the text (using Eqs. (14) and (15)), if we also introduce the particle acceleration efficiency  $\alpha$  as the only surviving effect of the  $\int \mathbf{E} \cdot \mathbf{B}$  term. A similar result shows that kinetically-driven hydromagnetic expansion is not impeded by magnetic turbulence [21]. As discussed in Appendix A2, expansion of the central column would be slowed down by accumulated mass giving  $v_A \ll c$ , often encountered in laboratory experiments but not for our disk model with  $v_A = c$ .

We now apply the above discussion to calculate the magnetic perturbation  $B_1$  representing entanglement of field lines. This  $B_1$  determines the electric field of Eq. (8) employed to discuss electron acceleration in Section 7 and ion acceleration in Section 8. We can estimate  $B_1$  from free energy due to magnetic relaxation trying to fill the vacuum region of Fig. 1A. For the radiolobe, with a limited duration  $\tau$ , relaxation extends only to

a radial gradient length  $R_1$  determined by magnetic diffusion due to the instability producing relaxation with a residual vacuum field outside  $r = R_1$ .

Free energy is liberated by unstable 3D perturbations  $\mathbf{B}_1$  giving as the total magnetic field:

$$\mathbf{B} = \langle \mathbf{B} \rangle + \mathbf{B}_1$$

where  $\langle \dots \rangle$  denotes the axisymmetric component, which is the field dealt with thus far in this paper. In principle, free energy is found by calculating the relaxed state at constant helicity satisfying:

$$\nabla \times \langle \mathbf{B} \rangle = \lambda \langle \mathbf{B} \rangle \quad (\text{A13})$$

$$\langle \mathbf{j} \rangle \times \langle \mathbf{B} \rangle = 0 \quad (\text{A14})$$

As is shown in Ref. [10], for a plasma connected to a helicity source,  $\lambda$  is not constant but instead falls from a peak value  $\lambda_1$  inside the central column to a lower value outside of order  $\lambda \approx 2/R_1$ , where, for a central column poloidal flux  $\psi_C$  and poloidal current  $I_C$ ,  $\lambda_C$  is given by:

$$\lambda_C = (\mu_0 I_C / \psi_C) = (\mu_0 I / \psi) = 2/a_0 \quad (\text{A15})$$

Because relaxation is ongoing and helicity is transported by  $\nabla \lambda$  [10], the  $\lambda$  profile is evolving in time. Here we avoid these complexities by noting that the pressure balance Eq. (A14) implies that any solution of Eq. (A13) gives the magnitude  $|\langle \mathbf{B} \rangle| \approx B(0)$  throughout the domain, where  $B(0)$  is the value at  $r = 0$ . Using this and the fact that  $\int \langle \mathbf{B} \rangle \cdot \mathbf{B}_1 = 0$ , we approximate the conservation of energy as:

$$\pi R_1^2 B_1^2 + \pi a_0^2 (B_0 - B(0))^2 = \pi a_0^2 B_0^2 [1 + \ln(R/a_0)] - \pi R_1^2 B(0)^2 [1 + \ln(R/R_1)] \quad (\text{A16})$$

The first term on the left hand side of Eq. (A16) represents tangled fields. While tangled field lines in 3D may be thinly distributed throughout the volume, as discussed in Section 6 and Appendix A3, their energy is concentrated within  $r < R_1 \approx (\nabla\lambda/\lambda)^{-1}$ , since diffuse lines of the same flux as that at  $r < R_1$ , in spreading out to  $R^*$  have an average amplitude reduced by  $(R_1/R^*)^2$  giving an energy less than the above by a factor  $[R^{*2}(R_1/R^*)^4/R_1^2] = (R_1/R^*)^2$ . The second term on the left is the approximate energy in coherent kink modes discussed in Section 9. The right hand side is the free energy, the first term being the unperturbed energy in Eq. (10), using Eq. (15), where here we retain the unity term concerning magnetic energy inside the column, versus the logarithmic vacuum term. The second term on the right includes the region  $r > R_1$  which is approximately a vacuum field despite a few loosely distributed field lines as noted above. We have canceled the common factor  $1/2\mu_0$  and we omitted the length  $L$ , giving then the energy line density. It is the fixed magnitude of this line energy density that reflects the limited free energy available in a column whose length freely expands, as noted above.

The significant feature in Eq. (A16) is that the vacuum field dominates the energy and only the symmetric states before and after a kink contribute much to the vacuum field. This follows from the fact that the symmetric vacuum vector potential is  $A_\phi \propto \ln(r/a_0)$  giving  $B_z \propto 1/r$  and energy  $\propto \ln(r/a_0)$ , while the vacuum field of kink perturbations (ideal or tearing) is dominated by  $A_z$  in  $\nabla \times (\nabla \times \mathbf{A}) = 0$  in vacuum giving  $A_z \propto r^{-m}$  for a mode with azimuthal wave number  $m$ , giving  $B_\phi \approx B_r \propto r^{-(m+1)}$  and an energy of order  $\pi a_0^2 (B_0 - B(0))^2$  (no log factor) as in Eq. (A16). This is true for any kink with  $k_z \ll m/a_0$ . Thus a transient coherent kink, in reducing  $B = B_0 - B(0)$  and hence its associated vacuum field, releases a large excess energy available to create tangled magnetic fields.

The radius  $R_1$  is given by diffusion caused by tangled magnetic field lines, giving approximately:

$$R_1^2 = Dt = ca_0 t (B_1^2/B(0)^2) \quad (\text{A17})$$

where  $t$  is the duration of  $B_1$  at peak amplitude. The diffusion coefficient  $D$  has two origins, each giving about the same magnitude of diffusion for our problem. First is



magnetic diffusion analogous to classical diffusion due to resistivity  $\eta$ , giving  $D = \eta^*/\mu_0$  where  $\eta^* = (E_{||}/j_{||})$  with  $j_{||} = (B/\mu_0 a_0)$  and  $E_{||} = v_A B(B_1/B_0)^2$  from Eq. (8) with  $v_A = c$ . A second origin for  $D$  is due to ion (and/or electron) flow parallel to the tangled field lines that occasionally nearly touch so that small effects can cause ions to jump from line to line. For relativistic ions with speed  $c$ , this transport, calculated by Rechester and Rosenbluth [22], again yields Eq. (18) but with  $d = L_C$ , the correlation distance between touching points. Actually these diffusion processes are additive, the first kind being diffusion relative to a reference frame fixed in the disk, the other relative to the field lines. Both give rise to  $E_{||}$ , which is to say that flow of particles parallel to tangled field lines accelerates these particles parallel to the symmetrized field lines.

Substituting Eq. (A17) into Eq. (A16) gives  $B_1$ . We solve the resulting equation as a quadratic in  $B_1^2$ , first treating  $\ln(R_1/a_0)$  as constant, to be iterated toward a solution:

$$(B_1/B(0))^2 = 1/2 X^* \{ -1 + [1 + 4(CX/X^*)]^{1/2} \} = C(X/X^*) \approx C \quad (\text{A18})$$

$$X = 1 + \ln(R/a_0) - (1 - B(0)/B_0)^2$$

$$X^* = 1 + \ln(R/R_1) = 1 + \ln(R/a_0) - \ln(R_1/a_0)$$

Here  $C$  is given by:

$$C = (a_0/ct)(B_0^2/B(0)^2) = (a_0/ct) (I^2/I_C^2) \quad (\text{A19})$$

where on the right we take  $B(0) = \mu_0 I_C / 2\pi a_0$  by Eq. (A15) and  $\Delta s$  is the interval along the current path over which turbulence described by Eq. (A17) applies. Eq. (A18) is valid for  $C \ll (X^{*2}/4X) \approx 5$  (allowing quite large fluctuations, the solution for larger  $C$  being  $\sqrt{CX}$ ).

We consider quasi-steady turbulence in the central column, taking  $t = \tau$  and  $I_C = I$ , yielding for numbers in Section 6:

$$(B_1/B_0) = \sqrt{C} = 10^{-6}, \quad \text{steady turbulence}$$

This result agrees with the value found to fit electron synchrotron data in Section 6, yielding an ion acceleration efficiency  $\alpha = 0.5$  in Table 1, Section 7.

Eqs. (A18) – (A19) are applied to transient acceleration in Section 9.

The condition for a local coherent kink to occur can be inferred from Taylor's discussion of coherent distortions of Reversed Field Pinches (RFP) in Ref. [23]. On approximating the RFP and spheromak as a straight cylinder [24], these conditions differ mainly in the fact that an externally applied toroidal field in the RFP allows greater freedom in the characteristic parameter  $\lambda = \mu \mathbf{j} \cdot \mathbf{B} / B^2$  whereby the relaxed state with minimum energy at fixed helicity, giving an eigenvalue  $\lambda \approx 2/a_0$  for spheromaks, can instead exceed  $\lambda = 3.2$  in RFP's, this being the threshold at which the lowest energy state is not symmetric but is instead a coherent kink as observed in RFP's [23]. A coherent kink can also form in the spheromak if  $\lambda$  is not constant inside the central column, as can happen because relaxation is not complete, as discussed in Appendix A2. An example is given in Ref. [24] for a cylindrical equilibrium with interior  $\lambda$  values up to  $\lambda = 5.5$ .

#### A7. Transport by Drift Cyclotron Modes

Ion acceleration discussed in Section 7 requires some means of diffusing ions preferentially across field lines. A likely candidate in the flux return is the drift cyclotron instability, in which ions (but not electrons) experience cyclotron resonance with the plasma waves. In this section we mainly focus on diffusion by drift cyclotron instability, with comments about the closely related filamentation instability at the end.

The threshold for the electrostatic drift cyclotron instability is discussed in Ref. [25] for a non-relativistic plasma. Here we discuss relativistic corrections and estimate transport rates.

For the drift cyclotron mode, the electron charge perturbation due to  $\mathbf{E} \times \mathbf{B}$  drift across a density gradient is unchanged by relativity, the perturbed drift velocity still being given by  $\mathbf{E}_1 + \mathbf{v}_1 \times \mathbf{B}_0 = 0$ . A term omitted here, given in Ref. [5], is order  $m_e/m_i$  (with relativistic masses), very small for our parameters. Then, for electrostatic modes (wavenumber  $\mathbf{k}$  parallel to  $\mathbf{E}_1$ ), the electron charge perturbation is obtained from the continuity equation:

$$-i\omega n_1 = -\nabla \cdot \{[(i\mathbf{k} \times \mathbf{B}_0/B_0^2)\Phi_1]n_0\} \quad (\text{A18})$$

Relativistic corrections to the ion charge perturbation for drift cyclotron modes require first replacing the cyclotron frequency by its non-relativistic value divided by  $\gamma_i$  both in calculating the resonant frequencies and the Larmor radius. To see this, we note that, for the ions, we can neglect the density gradient, giving plane waves with wave number  $\mathbf{k}$ . We linearize the relativistic Vlasov equation and for electrostatic modes we take the perturbation  $\mathbf{E}_1$  parallel to  $\mathbf{k}$ . Using Faraday's Law, we obtain, for frequency  $\omega$ ,  $\omega \mathbf{B}_1 = \mathbf{k} \times \mathbf{E}_1 = 0$  for electrostatic modes, hence no magnetic perturbation in the Lorentz force, and we may take  $\mathbf{E}_1 = -i\mathbf{k}\phi_1$ . The remaining complications concern integration over the relativistic ion orbit to obtain, by analogy with the non-relativistic case in Ref. [25]:

$$f_1 = n_0 e \phi_1 \int^t dt' i k_y (\partial f_{oi}/\partial p_y) \quad (\text{A19})$$

where we retain only a  $k_y$  component perpendicular to  $\mathbf{B}_0$  in the  $z$  direction (“flute-like” mode). In the regime of interest, where acceleration gives a roughly Maxwellian ion distribution  $f_{oi} \propto \exp(-E/T)$ ,  $(\partial f_{oi}/\partial p_y) = -(\partial E/\partial p_y)(f_{oi}/T) = -v_y(f_{oi}/T)$  just as in the non-relativistic case. Then the orbit integration procedure of Ref. [25] yields a drift cyclotron dispersion relation identical with the non-relativistic case, merely by substituting the relativistic cyclotron frequency, as stated above, and replacing integrals on  $\mathbf{v}$  by integrals on  $\mathbf{p}$ .

The other relativistic correction comes from  $T$  appearing in  $(\partial f_{oi}/\partial p_y)$  above, whereby, for Debye lengths calculated in terms of mass, the mass is really  $T$  and should be taken as the relativistic mass. If we substitute relativistic masses, we may still use the non-relativistic threshold for drift cyclotron instability, given in Eq. (148) of Ref. [25], giving instability if:

$$\epsilon r_{Li} > 0.4(\omega_{ci}^2/\omega_{pi}^2)^{2/3} \quad (\text{A20})$$

where  $\varepsilon = |\nabla n/n|$ . Here  $r_{Li}$  and the cyclotron and plasma frequencies should be calculated using the relativistic ion mass, giving, with the density from Eq. (4):

$$\omega_{pi}^2/\omega_{ci}^2 = (Ie^2/e\langle v \rangle A \varepsilon_0 m_i \gamma_i) (m_i^2 \gamma_i^2 / e^2 B_{TOR}^2) \approx (c^2/\langle v \rangle v_\perp) \varepsilon r_{Li} \quad (A21)$$

where  $v_\perp$  arises from introducing  $r_{Li}$ ,  $\varepsilon$  arises from  $A$  (either  $a$  in the central column or  $\Delta$  in the flux return) and  $a$  or  $r$  in  $A$  divided into  $I$  cancels one factor  $B_{TOR}$ . Substituting Eq. (A21) into Eq. (A20) gives for the instability condition:

$$\varepsilon r_{Li} > (\langle v \rangle v_\perp / c^2)^{2/5} \quad (A22)$$

This condition is not satisfied in the central column where  $\langle v \rangle = c$  but  $\varepsilon r_{Li} = (r_{Li}/a_o) = (v_\perp/c)^2$  with  $v_\perp/c = 10^{-4}$ . It is finally satisfied in the flux return just where it matters for our model, as  $r_{Li}/a_o \rightarrow 1$  giving  $\varepsilon r_{Li} \rightarrow 1$  and  $\beta \rightarrow 1$ , giving also  $v_\perp/c \rightarrow 1$  and  $\langle v \rangle/c \rightarrow (\Omega a_o/c)(E/eV) = 0.2(\gamma_i/\gamma_{MAX})$  by Eq. (39).

Eq. (A18) applies for a “loss cone” distribution empty at low ion energy. Since the basic drive for drift cyclotron modes is  $\mathbf{k} \cdot \partial f_o / \partial \mathbf{p}$  for the ions, saturation of the perturbation spectrum occurs when the rate of momentum diffusion filling in the “loss cone” matches the rate of ion escape via interaction of ion guiding centers with the electron drift waves, as discussed in Section 8 of the text. The radial and transverse diffusion coefficients in that discussion are related as follows.

Transverse diffusion by the  $\mathbf{E} \times \mathbf{B}$  drift wave motion gives:

$$D_T = \tau_{CT} (E_{Ir}/B_{TOR})^2 \quad (A23)$$

with correlation time  $\tau_{CT}$ . The energy diffusion coefficient is:

$$D_E = \tau_{CE} (d\varepsilon/dt)^2 = \tau_{CE} (ecE_{Ir})^2 \quad (A24)$$

where  $d\varepsilon/dt = cd p/dt = ce E_{Ir}$  for relativistic particles. Treating  $D_E$  as an effective “collision,” the radial diffusion coefficient is:

$$D_r = (D_E/(m\gamma c^2)^2)r_L^2 = \tau_{CE}(ecE_{Ir})^2(r_L/m\gamma c^2)^2 = \tau_{CE}(E_{Ir}/B_{TOR})^2 \quad (A25)$$

where  $r_L = (m\gamma c / eB_{TOR})$  and all parameters are for ions.

Comparing Eqs. (A23) and (A25), we see that, if the correlation times are about the same:

$$D_r \approx D_T \quad (A26)$$

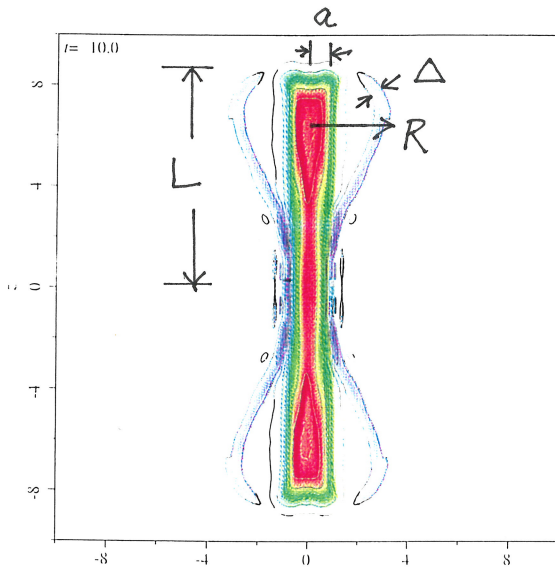
Since the  $D$ 's are comparable, and the radial density gradient gives a well-defined current velocity  $\langle v \rangle = D_r/r$  by Eq. (44), it follows that it is the transverse pressure gradient across the width  $\Delta$  that must adjust to bring about saturation of the turbulence. The density gradient also adjusts independently, in response both to density requirements to carry the current and squelching of the instability if too many ions accumulate at low energy to fill the “loss cone.” Density adjustments also affect the magnitude of  $|\nabla n/n|$  in Eq. (A20) and the orientation of  $\mathbf{k}$  in Eq. (A18).

Again, a correct calculation of ion transport sufficiently accurate to verify our ion diffusion model and also to yield the predicted cosmic ray energy spectrum requires Vlasov or PIC simulations.

## References:

- [1] Pierre Auger collaboration, *Science* **318**, 938 (2007).
- [2] M. C. Begelman, R. D. Blandford and M. J. Rees, *Rev. Mod. Phys.* **56**, 255 (1982).
- [3] S.A. Colgate and H. Li, *Comp. Rend. Physique* **5**, 431 (2004).
- [4] F. – Y. Chang et al., *Phys. Rev. Letters* **102**, 11101, (2009).
- [5] M. Nakamura, H. Li and S. Li, *Astrophys. J.* **652**, 1059 (2006).
- [6] C. R. Sovinec, J. M. Finn and D. del-Castillo-Negrete, *Phys. Plas.* **8**, 475 (2001).
- [7] D. Lynden-Bell, *Mon. Not. R. Astron. Soc.* **341**, 1360 (2003).

- [8] R. Krasnopolsky, Z-Y Li and R. Blandford, *Astrophys. J.* **526**, 631 (1999).
- [9] M. Lyutikov and R. Ouyed, *Astroparticle Phys.* **27**, 473 (2007).
- [10] T. K. Fowler and R. Gatto, *Phys. Plasma Control. Fusion* **49**, 1673 (2007).
- [11] D. D. Ryytov, R. H. Cohen and L. D. Pearlstein, *Phys. Plas.* **11**, 4740 (2004).
- [12] M. Nakamura, H. Li and S. Li, *Astrophys. J.* **656**, 721 (2007).
- [13] J. Finn, *Phys. Plas.* **12**, 092313 (2005).
- [14] J. D. Jackson, *Classical Electrodynamics*, J. Wiley & Sons, New York, Sec. Ed. Chap. 14.
- [15] G. R. Burbidge, *Astrophys. J.* **124**, 416 (1956).
- [16] R. J. Goldston and P. H. Rutherford, *Introduction to Plasma Physics*, Institute of Physics Publishing, Philadelphia, (1995), Chaps. 1, and 22.
- [17] G. V. Ustyugova, R. V. E. Lovelace, M. M. Romanova, H. Li and S. A. Colgate, *Astrophys. J.* **541**, L21 (2000).
- [18] A. H. Boozer, *Phys. Fluids* **29**, 4123 (1986).
- [19] D. C. Montgomery and D. A. Tidman, *Plasma Kinetic Theory*, McGraw-Hill, New York, (1964), Chapter 10.
- [20] W. E. Drummond and M. N. Rosenbluth, *Phys. Fluids* **5**, 1507 (1962).
- [21] T. O’Neil and T. K. Fowler, *Phys. Fluids* **9**, 2219 (1966).
- [22] A. B. Rechester and M. N. Rosenbluth, *Phys Rev. Letters* **40**, 38 (1978).
- [23] J. B. Taylor, *Rev. Mod. Phys.* **58**, 741 (1986).
- [24] D. D. Hua, T. K. Fowler and E. C. Morse, *J. Plas. Phys.* **66**, 275 (2001).
- [25] T. K. Fowler, “Mirror Theory”, *Fusion Part 1A*, E. Teller, Ed., Academic Press, New York, (1981).



T. K. Fowler 10/1/08

Figs. 4, 3, 11 Nakamura, Li, Li,  
Astrophys. J. **652**, 1059 (2006)

### Expansion

$$V = \Omega\psi, I = \psi/a, \psi = \pi a^2 B_z$$

$$dL/dt = (\Omega a / \ln R/a)$$

### Current-Limited Density

$$n = (j/ec), j = (I/A), A = \pi a^2 \rightarrow 2\pi r \Delta$$

### Synchrotron radiation, central column

$$I \delta V \propto \ln(\gamma B_z)^2 \propto I L (\gamma B_z)^2, \delta V/L = -\langle v \times B \rangle$$

### Example (MKS)

$$V = 3 \times 10^{19} = \text{cosmic ray}, I = 2.5 \times 10^{18}$$

$$a = 10^{12}, L = 10^{22}$$

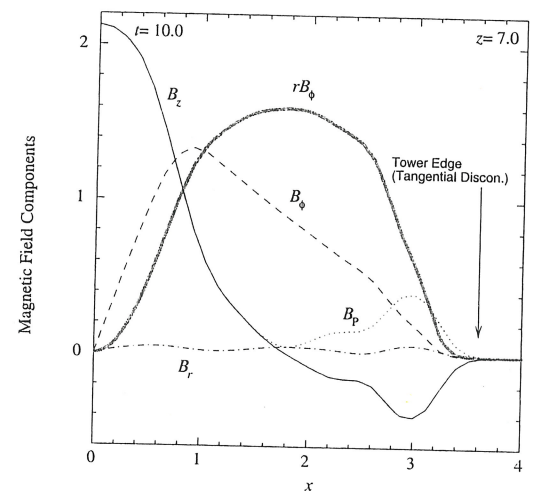
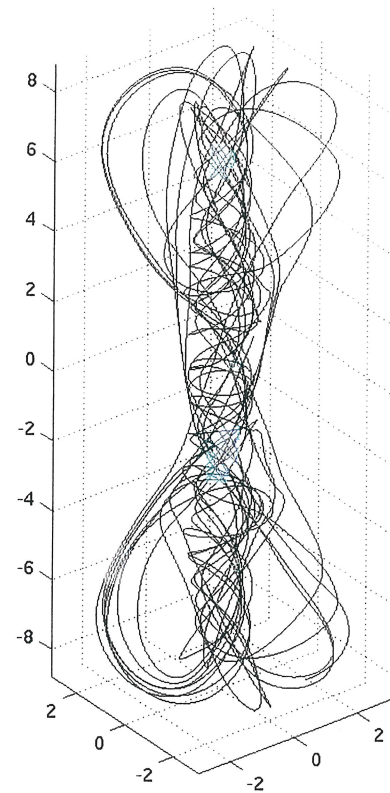
$$a\Omega = 0.2 c, \tau = 10 \text{ yrs}$$

$$IV\tau = 2 \times 10^{53} = 2 \times 10^{60} \text{ ergs}$$

$$B_z = 0.5, \lambda = 2 \text{ cm}, \gamma_e \approx 1$$

$$\delta V = 0.03 V$$

$$IV\tau = 2 \times 10^{53} = 2 \times 10^{53}$$



### Cosmic Ray Acceleration, flux return

$$\Delta \rightarrow \text{Larmor radius}$$

$$E_r = (V / r \ln R/a)$$

$$j_r = -D(dn/dr), D \approx c\Delta \text{ (drift cyclotron)}$$

$$N(E) \propto E^{-1}$$